TABLE OF CONTENTS (TOC)

High yield production of ultrathin fibroid semiconducting nanowire of Ta₂Pd₃Se₈

Xue Liu,^{1, 2} Sheng Liu,² Liubov Yu. Antipina,^{3, 5, 6} Yibo Zhu,⁷ Jinliang Ning,¹ Jinyu Liu,¹ Chunlei Yue,¹ Abin Joshy,¹ Yu Zhu,⁴ Jianwei Sun,¹ Ana M Sanchez,⁸ Pavel B. Sorokin,^{3, 5} Zhiqiang Mao,¹ Qihua Xiong,² and Jiang Wei*,¹

¹Tulane University, United States

²Nanyang Technological University, Singapore

³National University of Science and Technology "MISiS," Russian Federation

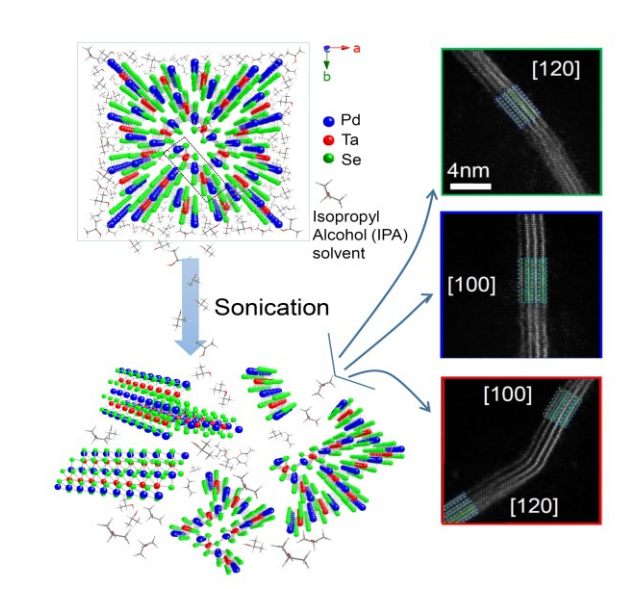
⁴The University of Akron, United States

⁵Technological Institute for Superhard and Novel Carbon Materials, Russian Federation

⁶Moscow Institute of Physics and Technology, Russian Federation

⁷Columbia University, United States

⁸Department of Physics, University of Warwick, Coventry, CV4 7AL, United Kingdom



Ultrathin semiconducting Ta₂Pd₃Se₈ nanowires down to a few "unit ribbons" have been produced via liquid phase exfoliation, showing highly preserved crystallinity and stability.

High yield production of ultrathin fibroid semiconducting nanowire of Ta₂Pd₃Se₈

Xue Liu,^{1,2} Sheng Liu,² Liubov Yu. Antipina,^{3,5,6} Yibo Zhu,⁷ Jinliang Ning,¹ Jinyu Liu,¹ Chunlei Yue,¹ Abin Joshy,¹ Yu Zhu,⁴ Jianwei Sun,¹ Ana M Sanchez,⁸ Pavel B. Sorokin,^{3,5} Zhiqiang Mao,¹ Qihua Xiong,² and Jiang Wei¹ (🖂)

- ¹ Department of Physics and Engineering Physics, Tulane University, New Orleans, Louisiana 70118, United States
- ² Division of Physics and Applied Physics, Nanyang Technological University, 637371, Singapore
- ³ National University of Science and Technology "MISiS," Moscow 119049, Russian Federation
- ⁴ Department of Polymer Science, The University of Akron, Akron, Ohio 44325, United States
- ⁵ Technological Institute for Superhard and Novel Carbon Materials, Moscow 108840, Russian Federation
- ⁶ Moscow Institute of Physics and Technology, Dolgoprudny 141700, Russian Federation
- ⁷ Department of Mechanical Engineering, Columbia University, New York, New York 10027, United States
- ⁸ Department of Physics, University of Warwick, Coventry, CV4 7AL, United Kingdom

Received: day month year
Revised: day month year
Accepted: day month year
(automatically inserted by
the publisher)

© Tsinghua University Press and Springer-Verlag Berlin Heidelberg 2014

KEYWORDS

Van der Waals nanowire, 1D semiconductor, liquid exfoliation, micro Raman spectroscopy, electronic and optoelectronic device

ABSTRACT

Immediately after the demonstration of the high-quality electronic properties in various two dimensional (2D) van der Waals (vdW) crystals fabricated with mechanical exfoliation, many methods have been reported to explore and control large scale fabrications. Comparing with recent advancements in fabricating 2D atomic layered crystals, large scale production of one dimensional (1D) nanowires with thickness approaching molecular or atomic level still remains stagnant. Here, we demonstrate the high yield production of a 1D vdW material, semiconducting Ta2Pd3Ses nanowires, by means of liquid-phase exfoliation. The thinnest nanowire we have readily achieved is around 1 nm, corresponding to a bundle of one or two molecular ribbons. Transmission electron microscopy and transport measurements reveal the as-fabricated Ta₂Pd₃Se₈ nanowires exhibit unexpected high crystallinity and chemical stability. Our low-frequency Raman spectroscopy reveals clear evidence of the existence of weak inter-ribbon bindings. The fabricated nanowire transistors exhibit high switching performance and promising applications for photodetectors.

1 Introduction

Van der Waals (vdW) two dimensional (2D) materials, such as graphene [1-3], hexagonal boron nitride (h-BN) [4], transition metal dichalcogenides

(TMDCs) [5-9] and black phosphorus [10] have attracted enormous research attention due to their extraordinary properties after thinning down to atomic level. Such high-quality mono or a-few-layer can be achieved with simple mechanical exfoliation, in which adhesive tape is used to effectively

Address correspondence to Jiang Wei, jwei1@tulane.edu



separate layers that are originally bonded by weak vdW interactions [1, 3]. The high crystalline films enable comprehensive studies of their novel quantum phenomena. Hidden behind the success of achieving these well preserved 2D film materials is the critical role of Van der Waals bond, weakly holding the layers together, but also chemically insert enough acting as a protective barrier to prevent degradation caused by the surface reaction. Moreover, the idea of mechanical exfoliation of 2D vdW material can be extended to one dimensional (1D) fibroid crystals, which consist of unit 1D molecular ribbons parallel bonded by vdW forces [11-17]. This presents a new path of fabricating TMDC nanoribbons and avoids the edge problems faced by traditional methods [18-21], in which nanoribbons are directly cut out from the 2D TMDC layers. Indeed, mechanical exfoliation has been successfully applied to exfoliate the vdW fibroid bulk crystal - Ta2Pd3Se8 (TPdS), which can be viewed as an assembly of parallel running zigzag molecular ribbon (also we called it chain in the text below) [11] with edges terminated by Pd atoms and bonded together with interchain vdW bonding. Nanowires composed of a few TPdS molecular chains as thick as a few nanometers have been achieved, demonstrating the feasibility of easy access to ultrathin high-quality 1D nanowires for studying their intrinsic properties as well as potential applications.

However, mechanical exfoliation method is limited only in small laboratory experiments due to the extremely low productivity. To produce large quantities or scales of nanostructures for more practical applications, researchers have made efforts to discover alternative methods. One typical technique, known as liquid-phase exfoliation (LPE), has been proposed to break vdW bonding by utilizing ultra-sonication assisted by chemical solvents. It has been demonstrated to be a scalable and effective method producing a large number of vdW nano-flakes from their bulk counterpart as mentioned [22-29], and carbon nanotubes from its bundles [30-33]. More interestingly, interactions are widely existing not only in 2D vdW crystals but also in fibroid 1D/quasi-1D vdW crystal systems. Broad fabrication of 1D nanowires is expected to be realized by extending these exfoliation methods from 2D to 1D vdW crystal systems.

Here we report on our LPE study of single-crystal 1D semiconducting TPdS fibroid nanowires. In particular, we find that by using the LPE method TPdS nanowires as thin as 1 nm to 4

nm can be efficiently produced. Our comprehensive studies through low-frequency Raman spectroscopy and high-resolution scanning transmission electron microscopy (STEM) demonstrate highly preserved crystal quality and weak inter-ribbon bindings. Then, the 1D nanowire transistors fabricated from liquid exfoliated TPdS show promising potential in applications, electrical switching and photoresponse photothermal dominated mechanism has also been revealed. Our work demonstrates a successful large-quantity fabrication of ultra-thin fibroid nanowires through a simple and clean technique. At this early stage, although semiconducting TPdS nanowires exhibit relative low mobility when compared to up-to-date record best carbon nanotubes [34-37] and silicon nanowires [38, 39], our fabrication method avoids the complexity caused by selection, separation, and protection problems remaining in current 1D system studies [40]. Besides, our STEM and transport results simultaneously indicate the outstanding stability of TPdS nanostructures even down to the nanometer scale, which is crucial for next-generation modern electronics.

2 Results and discussion

2.1 Exfoliations and basic characterizations

Ta₂Pd₃Se₈ belongs to the isostructure group of ternary chalcogenides $M_2X_3Y_8$ (M = Ta, Nb; X = Ni, Pd, Pt; Y = S, Se), which has a linear crystal structure with bonding strengths differ near 20 times between and within unit "ribbons" (the smallest repeating unit in crystal structure as highlighted by the dashed rectangular in Figure 1a [11]. For each ribbon, it contains two chains of edge-sharing Se trigonal prims centered by Ta atoms and bridged by Pd atoms. The chains are further capped by additional Pd atoms at the two sides. The lateral dimension of one unit ribbon is 1.0 nm × 0.4 nm. The ribbons are interconnected via bindings weak between terminated-Pd (trans-Se) atoms and trans-Se (terminated-Pd) atoms with neighboring ribbons, forming a windmill shape framework extending along c-axis. From the crystal structure, we believe that the existence of isotropic vdW bonds in TPdS crystal is crucial for successful isolation of ultrathin nanostructures or even single molecular chain out from the bulk counterparts. In the LPE process, a powerful sonication is applied to effectively break

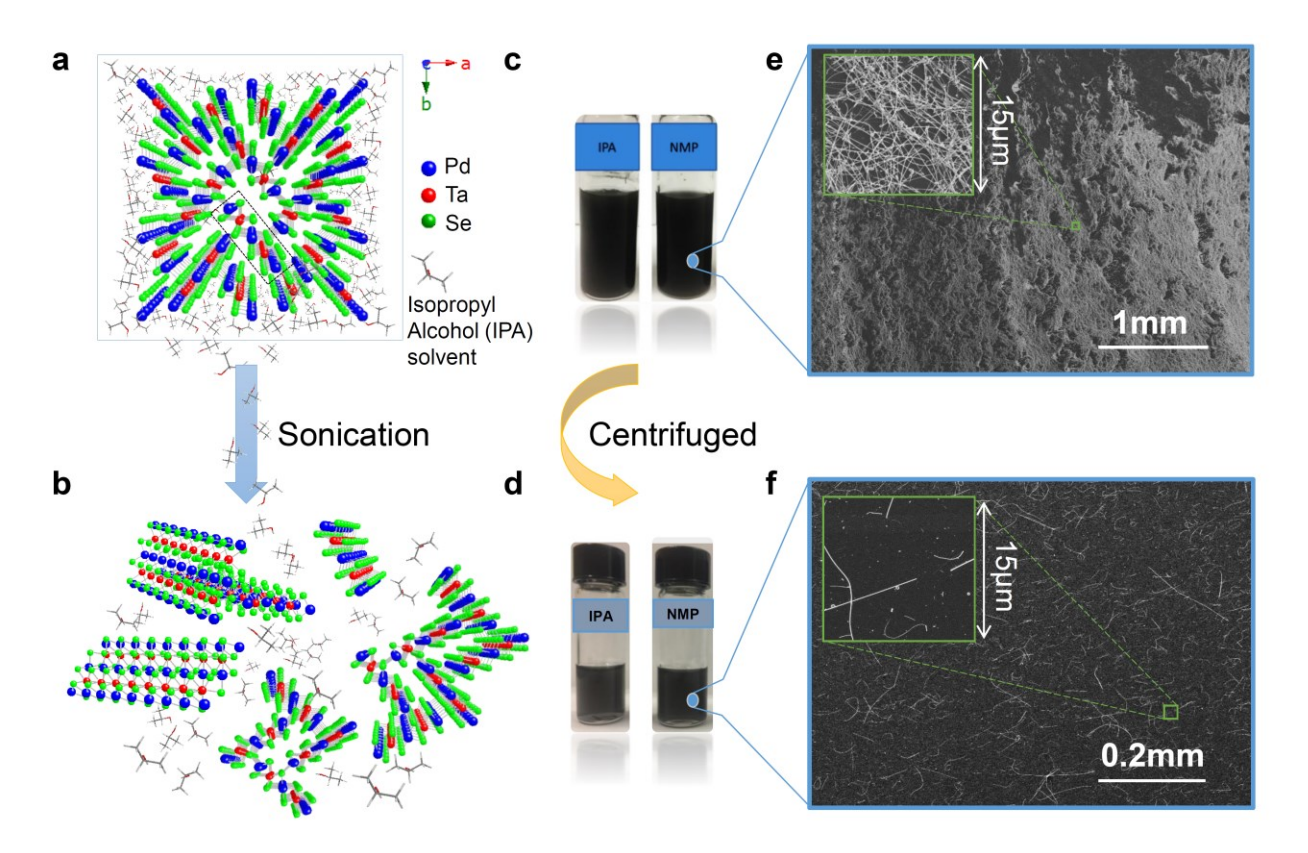


Figure 1 Crystal structure and exfoliation results. (a) Stereo-view of Ta₂Pd₃Se₈ bulk crystal structure along the *c*-axis. Note, we use unit ribbon to describe the smallest repeating unit in our Ta₂Pd₃Se₈ crystal structure. (b) Simulated Ta₂Pd₃Se₈ nano-structures achieved by ultra-sonication exfoliations with the assistance of chemical solvents (IPA). (c) Ta₂Pd₃Se₈ dispersions in IPA and NMP solvents right after sonication. (d) Resultant liquids after 1 hour's centrifugation at 500 rpm for IPA and NMP. (e), (f) Scanning Electron Microscopy images of Ta₂Pd₃Se₈ nanowires deposited on Si wafer using liquids from (c) and (d), respectively. Inset, SEM zoom-in view of the selected 15 μm×15 μm square.

the inter-ribbon interactions so as to obtain separated thin nanowires, as illustrated by Figure 1b. To process the exfoliation, we surveyed different including isopropyl alcohol solvents, N-methyl-2-pyrrolidone (NMP), chloroform, etc. (see Supplementary Figure 1 and Supplementary Table 1). The bulk TPdS crystal of 0.5 mg was immersed into different solvents (20 ml) and then ultra-sonicated for 4 hours at 50°C with a total input power of 0.6 MJ. After analyzing the exfoliation results, we note that NMP and IPA were the most appropriate solvents resulting in TPdS nanowires dispersions as shown in Figure 1c, and NMP mixture was more stable without significant reaggregation after a few hours. The different exfoliation processes are supposed to be closely related to their surface tension and corresponded dispersive and polar components matching with our TPdS nanowires [41]. We suggest

the NMP with a surface tension of 40.79 mJ·m⁻² and polar component/dispersive component ratio of ~ 0.4 match better with the TPdS nanowires (see Supplementary Note 1). The sonicated mixtures were then centrifuged at 500 rpm for 1 hour, the sediment was weight as ~21 wt% of the initial bulk material, and the supernatants were collected as the resultant liquids indicated by Figure 1d. We performed further characterizations based on deposited nanowires on a substrate (SiO₂/Si wafer), referred to as on-chip sample (see Methods). Figure 1e and 1f show the as-prepared samples (NMP solvent) under Scanning Electron Microscopy (SEM) before and after centrifugation, respectively. Before centrifugation, the TPdS nanowires were densely overlapped on the wafer. After centrifugation, individual nanowires with random orientations can be easily found.

From our observation, there is no significant

un-separated or aggregated big chunk of crystals after exfoliations. This indicates that the bulk TPdS been become extensively separated and with certain thickness nanowires and length distributions. Then, we systematically investigated the thickness and length distributions of the nanowires produced by IPA and NMP solvents using Atomic Force Microscopy (AFM). As shown in Figure 2a and 2b, a variable range of thicknesses and lengths of TPdS nanowires are demonstrated by the AFM images of randomly selected areas from IPA and NMP samples, respectively. Zoom-in views of 5×2.5 μm² squares indicate TPdS nanowires as thin as 1.4 nm can be readily achieved. It is worth noting that the thinnest nanowire observed from our AFM is ~1 (Supplementary Figure 4), which should

correspond to nanostructures consisting of 1-2 unit molecular chains as compared with the simulation (see Supplementary Figure 3). To better compare the results, the contour plots of the histograms of the nanowire thickness and length distributions, as obtained from 400 individual nanowires, are shown in Figure 2c and 2d for IPA and NMP exfoliations respectively. Both of the IPA and NMP exfoliated nanowires have thicknesses that are most distributed (> 90% number fraction) below 10 nm, while the NMP exfoliation yields slightly thinner and shorter nanowires in average, for which we can achieve ~45.57% nanowires below 4 nm. We also estimated the mass fractions of different thicknesses after centrifugation (see Methods). The mass fraction for nanowires below 10 nm is 48.3 wt%, and 4.8 wt% for

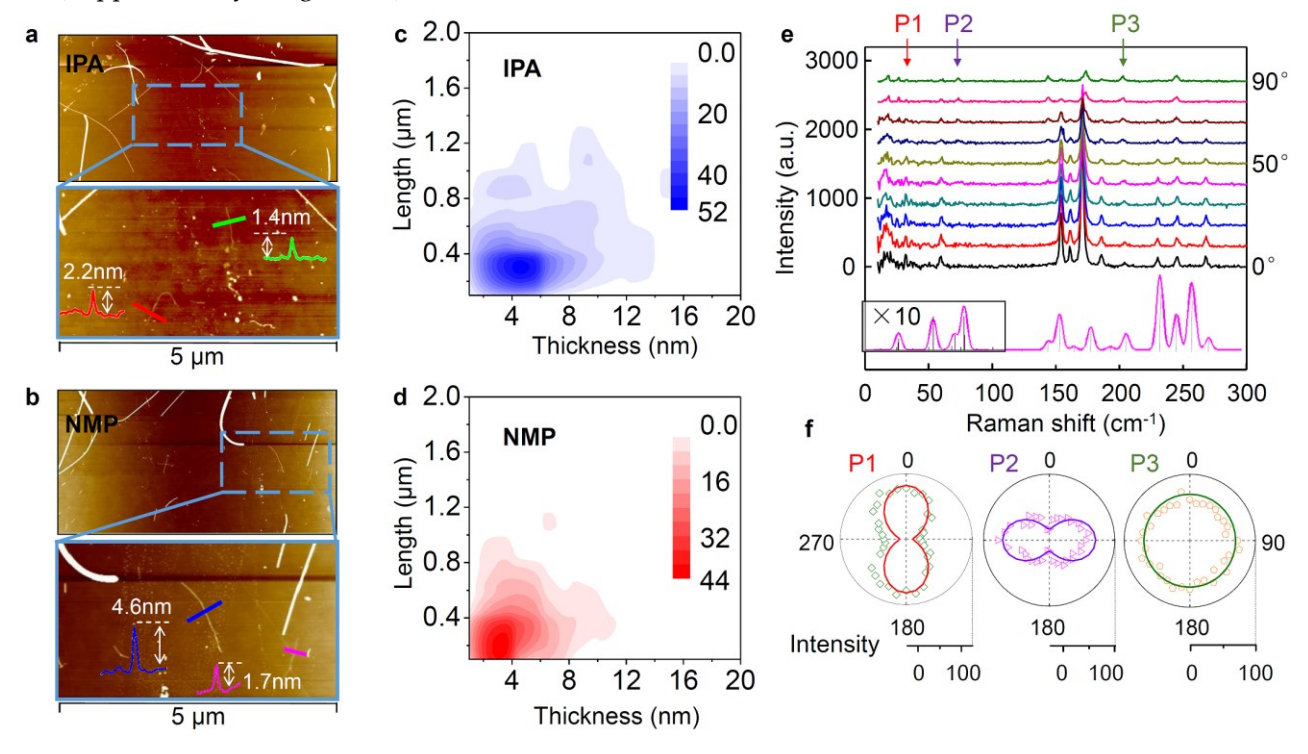


Figure 2 Basic characterizations of exfoliated nanowires. (a), (b) Atomic Force Microscopy images of the on-chip deposited Ta₂Pd₃Se₈ nanowires exfoliated using (a) IPA and (b) NMP solvents, respectively. Insets in the zoom-in view of selected areas (dashed blue rectangular 5 μm × 2.5 μm) show height profiles of four individual nanowires, indicating thicknesses of 2.2 nm, 1.4 nm, 4.6 nm, and 1.7 nm. (c), (d) Contour plots of the thickness and length distributions of the Ta₂Pd₃Se₈ nanowires produced by (c) IPA and (d) NMP solvents, respectively. (e) Raman spectra of a thick (~1 μm) TPdS fiber under different excitation polarization. 0° and 90° denote parallel and cross-polarization configurations respectively. Note, the stimulated Raman spectrum has been plotted at the bottom for comparison, the low-frequency part from 0 to 100 cm⁻¹ has been multiplied by a factor of 10. (f) Raman intensity polarization dependence for P1 (32.5 cm-1), P2 (72.9 cm-1), and P3 (201.5 cm-1), respectively. Scattered points: measured peak intensity. Solid lines: guidelines for the polarization patterns.

nanowires below 4 nm. Thus the total yield from the initial material can be estimated as 38.2% for nanowires below 10 nm and 3.8% below 4 nm. Our following discussions are all based on NMP prepared sample. We would like to note that for low-wavenumber Raman spectroscopy and electrical device measurements, we focused on relatively thick TPdS nanowires so as to obtain strong signals for the Raman spectra and achieve good contacts for electrical devices.

2.2 Low-wavenumber Raman spectroscopy and transmission electron microscopy studies

Based on the on-chip deposited nanowires, we performed low-wavenumber Raman spectroscopy study (see Methods). Vibrational modes located at low-wavenumber range less than 100 cm⁻¹ can denote the movement of atoms or molecules governed by weak forces, including vdW, quasi-vdW, and Low-wavenumber hydrogen bond. Raman spectroscopy has been successfully used to investigate the interlayer phonon modes in 2D materials [42] and the intermolecular interactions between aromatic molecules [43-45]. Our detailed Raman spectroscopy studies provide guidance for further understanding of one-dimensional crystal structure and symmetries. As shown in Figure 2e, different Raman spectra at polarization configurations for a relatively thick nanowire (diameter ~1 µm), have been stacking plotted together. We measured the excitation-angle dependencies of the Raman peaks, where 0° and 90° represent parallel (z(xx)z) and cross (z(yx)z)polarization configurations. A few peaks in the low wavenumber region (<100 cm⁻¹) are examined under different configurations, i.e. 18.1 cm⁻¹, 26.9 cm⁻¹, 32.5 cm⁻¹, 60 cm⁻¹, and 72.9 cm⁻¹ can be clearly resolved at (z(yx)z)configuration. The successful demonstrations of low wavenumber Raman peaks indicate the existence of inter-chain vibrations in our TPdS system. In addition, these measured Raman peaks exhibit distinct excitation-angle dependent polarizations, as demonstrated by the intensity polarization angle dependences in Figure 2f. Here, we take P1 (32.5 cm⁻¹), P2 (72.9 cm⁻¹), and P3 (201.5 cm⁻¹) as the examples of these different polarizations. More specifically, the Raman intensity of P1 is

consistent with the laser polarization, which reaches a maximum at the parallel configuration and a minimum at the cross configuration. In contrast, P2 intensity shows the opposite evolution, and P3 intensity stays almost constant. These different polarization dependences indicate distinguishable symmetries related to these Raman modes [42, 46]. Since the detector polarization is aligned with our TPdS chain direction, vibrations along the chain and totally symmetric vibration modes will preserve the laser polarization in Raman scattering. Therefore, we can see that the P1 mode reflects the breathing-like vibration between chains or shearing-like vibration along the chain, and the P2 mode corresponds to the shearing-like vibration perpendicular to the chain. P3 mode shows a slightly broader peak, which may correspond to a combination of two vibrations with close energy. One is mainly on the chain direction, and the other consists of a significant component perpendicular to the chain. We have simulated the possible corresponded atoms vibration modes, as shown in Supplementary Figure 5 and Figure 6. However, due to the complexity of the crystal structures, we are not able to correlate the irreducible representations for these peaks, which is beyond the scope of this research work. In fact, we also performed a simulation of Raman spectra evolution with different thicknesses, as can be seen in Supplementary Figure 7, only single and double ribbons produce unique spectra. For example, in Raman spectra of a single ribbon, the modes corresponded to the vibration of the bonds between ribbons are absent. With increasing nanowire size, its Raman peaks tend to the bulk spectrum.

To further analyze the crystallinity of the exfoliated **TPdS** nanowires, we preformed aberration-corrected scanning transmission electron microscopy (STEM) characterization. High-quality nanowires with various thicknesses can be easily identified. Figure 3a shows annular dark-field (ADF) images of a thicker (9.3 nm) TPdS nanowire along the <100> zone axis. The orientation can be corroborated by the fast Fourier transform (FFT), as indicated by the top right inset. The interplanar distances correspond with the (100), (2-11), and (2-10) planes (compared with the result of crystal structure simulation). The atomic resolution image of the TPdS nanowire clearly shows a smooth and clean surface

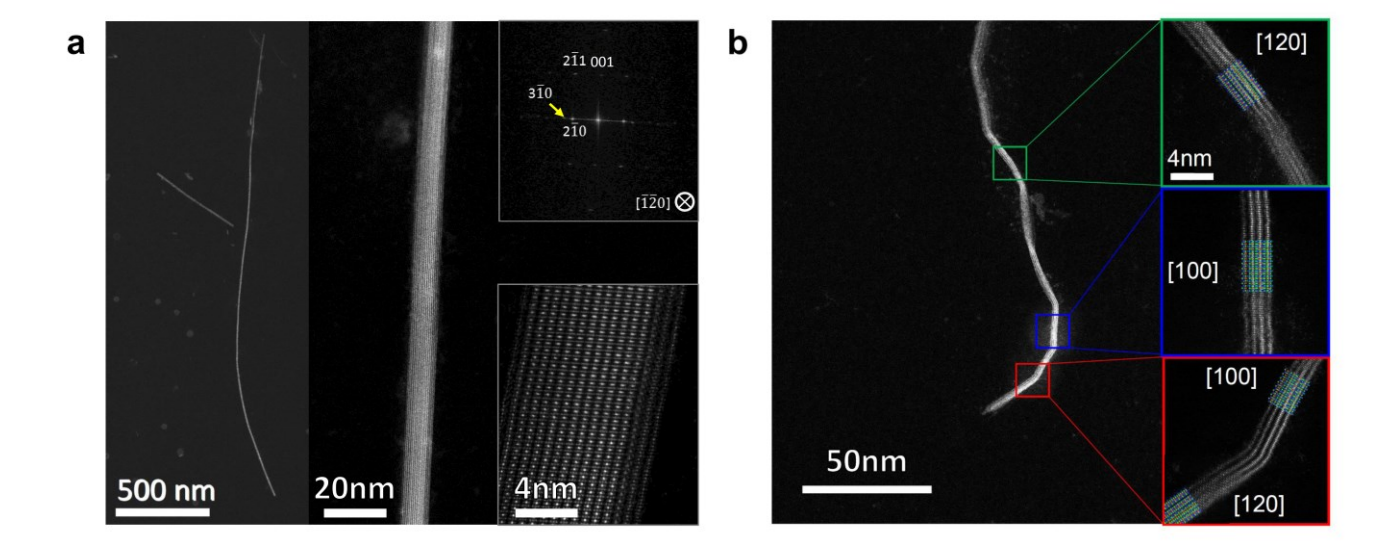


Figure 3 High-resolution Scanning Transmission Electron Microscopy studies. (a) Annular dark-field (ADF) transmission electron microscopy images of a thicker (9.3 nm) Ta₂Pd₃Se₈ nanowire along the <100> zone axis. From left to right, ADF images of the same nanowire with increasing magnifications show the uniformity and smooth surface. Top right inset: fast Fourier transform pattern of the selected area. (b) ADF images of an ultra-thin (3.2 nm) Ta₂Pd₃Se₈ nanowire. Left: low magnification image shows the nanowire curvature. Right: atomic resolution images of three selected areas. Note: simulated crystal structures have been fitted perfectly with STEM images.

without significant degradations, as shown by the bottom right inset of Figure 3a. Figure 3b shows the ADF images of an ultra-thin (~3.0 nm) TPdS nanowire. The nanowire shows a few segments orientated in different directions, as highlighted in the image. At a higher magnification, we observed atomic resolution images of this specific nanowire at three selected areas. The crystal orientation can be identified by comparing it to the simulated crystal structure with six-unit chains, as shown by Figure 3b inset. The view directions of area 1 and area 2 are [120] and [100], respectively. Area 3 shows a twist of the nanowire from [100] to [120]. The TEM analysis beyond both thicker and ultra-thin TPdS nanowires indicates an extremely high level of crystallinity, which has been successfully preserved during the LPE process.

More interestingly, we didn't observe a significantly oxidized or amorphous layer on the exfoliated nanowires even after storing in an ambient environment for more than one month. This phenomenon is consistent with our calculations of H₂O and O₂ adsorptions on TPdS surface, as shown by Supplementary Figure 10. For the TPdS crystal,

the adsorption energy for O₂ molecules is 1.12 eV/molecule, indicating adsorption of O₂ is not favorable. Although the TPdS surface shows favorable adsorption of H₂O molecules with an adsorption energy of -0.33 eV/molecule, the TPdS structural geometry is stable upon such adsorption as indicated by Supplementary Figure 10. In fact, this stable crystal structure at a nanometer scale is crucial for modern electronic applications. Thus, we further characterize the device performance based on high-quality TPdS nanowires.

2.3 Functionality demonstrations and zero-bias photoresponse

It has been demonstrated that the mechanical exfoliated TPdS nanowire is a good candidate for the channel material of 1D field-effect transistor [11]. In order to study the electronic transport properties of TPdS nanowires through LPE method, we fabricated FETs with a double-gate layout. As indicated by Figure 4a, a DC current is flowing through TPdS nanowire which is tuned by a back gate and a top ionic liquid gate separately (Ionic liquid N,N-diethyl-N-(2-methoxyethyl)-N-methylammoniu

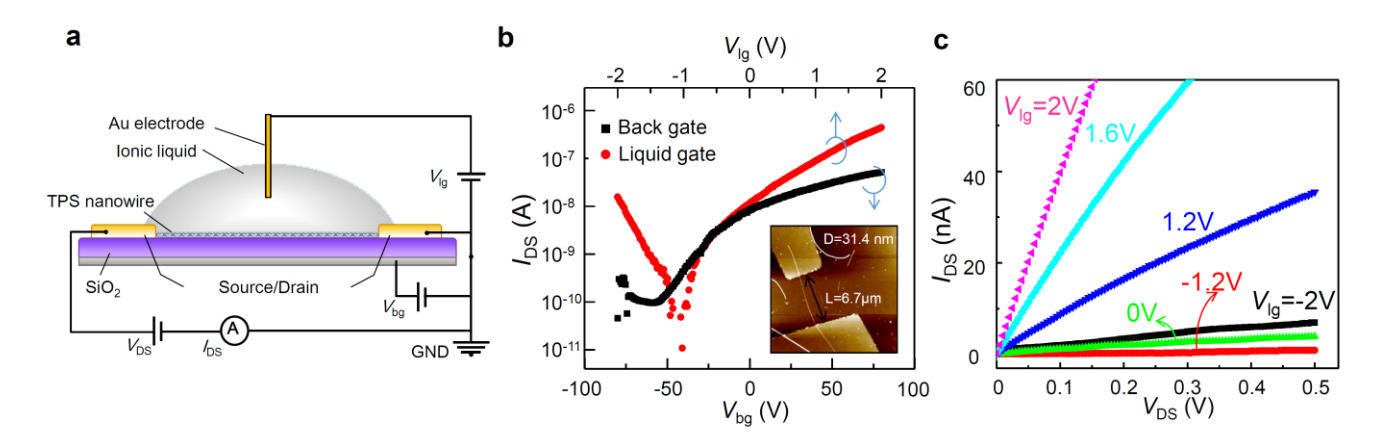


Figure 4 Transport properties for the fabricated 1D-transistors. (a) Schematic drawing for the fabricated Ta₂Pd₃Se₈ nanowire field-effect transistor with a double-gate setup. (b) Transconductance gate dependence for a typical field-effect transistor based on a 31.4 nm nanowire. Red and black dots are linked to top (ionic liquid gate voltage) and bottom (back gate voltage) axis, respectively. Inset: atomic force microscopy image of the measured nanowire device. (c) *I*_{DS}-*V*_{DS} sweeps at different liquid gate voltages, 2 V, 1.6 V, 1.2 V, 0 V, -1.2 V, and -2 V. Note, the liquid gate and back gate are applied separately.

m bis (trifluoromethylsulphonyl) imide (DEME-TFSI) has been used as the gate medium) [47]. Figure 4b shows the transconductance for a typical FET based on a 31.4 nm TPdS nanowire, as indicated by the AFM image (Figure 4b inset). Under the back gate, at a source-drain bias of 0.5 V, the TPdS nanowire clearly shows n-type semiconducting behavior. The device can be switched to on-state with $I_{\rm DS} = 5.1 \times 10^{-8}$ A at $V_{\rm bg}$ =80 V, and turned into off-state with $I_{\rm DS} < 1 \times 10^{-10}$ A at $V_{\rm bg} = -50$ V, resulting in an on/off ratio larger than 500. Based on the back gate sweeps, the field-effect mobility μ_{EF} can be extracted from the standard FET model:

$$\mu_{EF} = \left[\frac{dI_{DS}}{dV_{bg}} \right] \times \left[\frac{L}{WC_{ox}V_{DS}} \right].$$

Here, L is the channel length of 6.7 µm, and W is the channel width of 31.4 nm. Cox is the capacitance per unit area, which can be determined $C_{ox} = \varepsilon_r \varepsilon_0 / d_{ox}$, where ε_0 is the dielectric constant of vacuum, ε_r represents the relative dielectric constant of 3.9 for SiO₂, and d_{0x} is 300nm as the dielectric layer thickness. For this specific device, μ_{EF} equals to 32.5 cm²V⁻¹s⁻¹ at V_{bg} = 80 V, which is comparable with that achieved through mechanical exfoliated TPdS nanowire (with an average of 80 cm²V⁻¹s⁻¹). Our TPdS nanowires exhibit comparable or even better performance compared with other solution-processed semiconducting nanostructures, i.e. MoS₂ [48], black phosphorus [26, 49], and carbon

nanotubes [33, 50, 51] (see Supplementary Table 3 for detailed comparisons). To further improve the gate response of the TPdS FETs, a top ionic liquid gate is applied in a range of -2 to 2 V when the back gate is grounded instead. The device shows significant bipolar behavior with an on-current of 4.5×10^{-7} A at the electron side and 1.4×10^{-8} A at the hole side. The off-state current is as low as 10^{-10} A, indicating a higher on/off ratio near 10^4 . The swing slope extracted from the gate sweeps has been improved from 23 V/dec for back gate to 517 mV/dec for ionic liquid gate. Figure 4c shows the linear I_{DS} - V_{DS} dependence at different liquid gate voltages from -2 to 2 V, indicating nearly ohmic contacts between TPdS nanowire and the gold metal.

Then, we further checked the stability of our TPdS nanowires from the transport analysis. As shown in Supplementary Figure 11, the 1D TPdS transistor shows very good stability with almost unchanged transconductance after stored in an ambient environment for more than two months. We believe that the oxidation process is quite slow since it will increase the resistance or make the contacts worsen significantly. This result is in good consistency with our STEM studies and theoretical calculations, as discussed above. They have simultaneously provided solid supports for the good stability of our TPdS nanostructures.

From the above analysis, our exfoliated TPdS

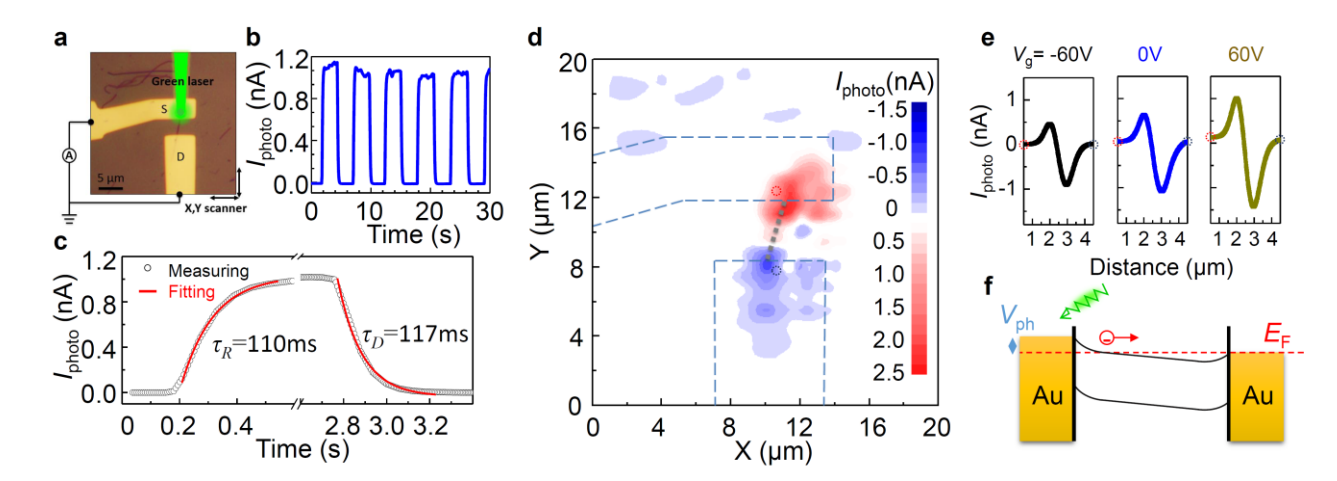


Figure 5 Photoresponse study based on Ta₂Pd₃Se₈ transistors. (a) Optical image of the fabricated nanowire device and schematic drawing for the photocurrent mapping setup. The laser used in this experiment is 532nm solid laser. (b) Room-temperature photoresponse with a few lights on/off cycles based on the device in (a). Note: the source-drain bias has been set to zero. (c) Zoom-in view of one cycle showing the rise and decay processes. Black dots: measured photo-response curve. Red solid line: fitted curve with exponential decay function. (d) Photocurrent mapping contour plot based on the device in (a). (e) Gate dependent photocurrent profiles across the line-cut starting from red dashed circle to the blue dashed circle in (d), from left to right, the back gate voltage is set to -60 V, 0 V, and 60 V. (f) Band diagram of the photothermalelectric mechanism.

nanowires exhibit outstanding semiconducting properties. In such a quasi-1D semiconducting system, its promising application as photodetectors is worth being pursued [52-57]. Our following discussions will focus on the photo-response study based on TPdS nano-devices. Figure 5a shows the optical image of a two-terminal photodetector device. Under our confocal microscope system, the 532 nm green laser as the excitation light was focused at the center of the device. A typical time-resolved photoresponse is plotted in Figure 5b, Iphoto at zero source-drain bias rises upon turning on the laser and decays after switching off the laser. As shown by the rise and decay process in Figure 5c, the response curve can be characterized by a single exponential function expressed as

$$I_{photo} = A_0 \times \exp(-(t - t_0) / \tau) + B_0,$$

where t_0 is the time when the laser is switched on, A_0 and B_0 are fitting constants, and τ is the time constant. The fitted time constants for rising (τ_R) and decay (τ_D) processes are 110 ms and 117 ms, respectively. Actually, there have been intensive studies on the photoresponse of a wide range of low dimensional materials. The response time varies significantly for different materials. For example, the rising and decay

time is 1.5 ps in graphene [58], ~1 ms in black phosphorus [59], and ranging from 5 ms to 4 s in TMDC thin flakes [60-64]. It is worth noting that, even in the same material, such as MoS2 monolayer [60, 63], the rising and decay time shows inconsistency, implying dominated mechanisms may be different for different samples or materials. In semiconducting photodetectors, nanoscale different mechanisms have been identified, including the photovoltaic effect and the photothermoelectric effect. The response time in the latter process is generically limited by the phonons since heat transfer is the essential step. On the other hand, the response speed also can be significantly affected by external factors, i.e., in disorder rich metal oxide nanowires such as ZnO, Nb₂O₅, Cu₂O, etc., the rising and decay time can be as long as 100s due to surface trapping and disorders [65, 66]. Our previous study based on mechanical exfoliated TPdS nanowires has reported a variable range hopping dominated transport, which indicates the disorder and surface trapping play an important role in device properties [11]. Thus, the disorder and surface trapping states may cause trapping of photoexcited carriers, which is expected to contribute to the slow response for our TPdS photodetectors.

In order to explore the photocurrent generation mechanism, we presented scanning photocurrent microscopy measurements on our TPdS device (see Methods). Figure 5d shows the 2D contour plot of the photocurrent depending on the laser spot (~ 1 µm diameter) locations at the device (see Supplementary Note 2 for laser spot determination). photocurrent exhibits a sign switching when the laser spot is scanned from source to drain electrodes, with maximum magnitudes at these metal-semiconductor contact edges. Besides, when the laser spot is located micrometer away from these two edges, either in-between or at the two sides, the photocurrent is still existing but with smaller magnitude. This is in controversy with the p-n junction or Schottky barrier driven photovoltaic effect, which is supposed to be constrained at the p-n or metal-semiconductor interfaces [67, 68]. However, it can be explained by the photothermoelectric effect because the laser heats the metal contacts and generates temperature differences and gradients. This laser heating is generally existing and not a negligible effect in microscopy experiments. The local temperature of gold contacts can easily rise about 0.4 K even with a laser heating power as low as 60 µW [69]. Besides, we all the measurements performed temperature when the Schottky barrier in our TPdS transistor is negligible, as evidenced by the linear IDS-VDS curves in Figure 4c. Thus, we propose a photothermoelectric effect dominated mechanism in our TPdS 1D photodetector, as illustrated by Figure 5f. In particular, a local temperature gradient induced by light absorption drives electrons to travel through the device. When the laser is heating up the contacts, the Seebeck coefficient difference between Au metal and TPdS nanowire generates a photothermal voltage across the junction, which could explain the maximum photocurrent observed at the contact edges but not only constrained there [69-72]. Meanwhile, shown in Figure as Supplementary Figure 14, the photocurrent profile along the line-cut from the red to blue dashed circles in Figure 5d does not show clear gate dependence, which provides evidence for the photothermal dominated mechanism as the photovoltaic effect should depend on the band alignments significantly [52, 73].

3 Conclusion

have demonstrated the In summary, we large-quantity production of high-quality ultra-thin TPdS nanowires using liquid-phase exfoliation with selected solvents. The resultant TPdS nanowires show highly preserved crystallinity and can be considered as an important step toward the fabrication of perfect 1D TMDC nanoribbons with naturally semiconducting properties. 1D field-effect transistors based on exfoliated TPdS nanowires exhibit competitive electrical transport properties and high mobility among liquid exfoliated van der Waals semiconductors. Besides, the as-fabricated devices show significant photoresponse with a clear photothermal dominated mechanism. Our work sheds light on the extension of the wet exfoliation technique to 1D or quasi 1D van der Waals materials, which contains a large group of candidates. The efficient production of 1D semiconducting TPdS nanowires can provide a wide range of applications, referred 1D field-effect transistor, optoelectronics, energy harvesting, chemical sensing, and biological sensing, etc.

4 Methods

4.1 Bulk synthesis

Bulk Ta₂Pd₃Se₈ single crystal is synthesized using Chemical Vapor Transport method. The mixture of thoroughly ground stoichiometric Ta, Pd, and Se element powders was sealed in a quartz tube under vacuum and pre-heated for a week at 750 °C. The resultant powder was ground again and sealed in a new tube together with 75 mg iodine (transport agent). Then the tube was put into a double zone furnace with the charge end and the other end heated up to 850 °C and 900 °C, respectively. The temperature was reversed with charge end at 900 °C and cold end at 850 °C after one day, and the reaction lasted for one week. After the furnace shut down, long needle-like single crystals with silver luster were formed at the cold end.

4.2 Sample preparations

Part A, liquid form sample preparations. 0.5 mg bulk TPdS single crystal was immersed in 20 mL solvents (IPA or NMP). The mixture was sonicated

for 4 hours at a bath temperature of 50 °C. The obtained dispersion was centrifuged at 500 rpm for 1 hour, and the top half of the centrifuged solution was collected as the liquid form sample.

Part B, on-chip sample preparations. The on-chip samples were prepared using drop-casting methods. The substrate is 1 cm² square Si/SiO₂ (300 nm) wafer. The solution was drop cast on the substrate and dried by using a spin-coater to spin at 1000 rpm for 10 seconds. Then, the samples were rinsed in IPA for 2 mins and dried by using compressed air.

4.3 Characterizations

Raman scattering spectroscopy measurements were carried out at room temperature using a micro-Raman spectrometer (Horiba-JY equipped with liquid nitrogen cooled charge-coupled device (CCD). The measurements were conducted in a backscattering configuration under a triple subtractive mode, excited with a diode green laser (λ = 532 nm). We used a reflecting Bragg grating followed by another ruled reflecting grating to filter out the laser sidebands, and as such, we can achieve the limit of detection ~5 cm⁻¹. The backscattered signal was collected through a 100x objective and dispersed by an 1800 g/mm grating with a spectral resolution of 0.7 cm⁻¹. For polarization measurement, we fix the analyzer before the detector and the sample and rotate the polarization direction of the laser excitation.

SEM was performed using Hitachi S-4800 FESEM. The images under all magnifications were acquired at 5 kV acceleration voltage. 1 nm thick carbon layer was uniformly deposited on the samples to reduce the charging effect caused by the SiO₂ substrate.

Atomic resolution ADF-STEM images of TPdS nanowires were obtained using a JEOL annular field detector with a fine-imaging probe. The probe current was approximate 23 pA with a convergence semi-angle of 22 mrad and an inner semi-angle of 45-50 mrad.

4.4 Mass fraction and yield estimations

The mass fraction of the exfoliated Ta₂Pd₃Se₈ nanowires can be estimated according to our AFM length and thickness distribution analysis. Given that

the volume of an individual nanowire is assumed as $V=\rho D^2 L$, where D is the diameter (thickness), L is the length, and ρ is the density, the mass fraction of individual thickness can be estimated as:

$$F = \frac{\sum_{individual} D_{ind}^2 L_{ind}}{\sum_{all} D_{all}^2 L_{all}}.$$

Then, since the sediment after centrifugation (500 rpm, 1 hour) has been weight as ~21 wt% of the initial bulk material, which indicates ~79 wt% remaining in the supernatant used for the AFM analysis. The total yield from the initial bulk TPdS crystals can be calculated as $Y=F \times 79\%$.

4.5 Raman active vibration modes simulations

All calculations of the atomic and electronic structure of Ta₂Pd₃Se₈ nanowires were performed using a density functional theory [1, 2] within the PBE-PAW approximation [3] with the periodic boundary conditions using a Vienna Ab-initio Simulation Package [4 - 6]. The plane-wave energy cutoff was equal to 300 eV. For the calculation of the equilibrium atomic structure, the Brillouin zone was sampled according to the Monkhorst–Pack [7] scheme with a grid not less than 4×6×10 k-point for bulk structure and 1×1×12 k-point for quasi 1D nanowires structures. The structural relaxation was performed until the forces acting on each atom were less 0.01 eV/Å.

The Raman spectra spectrum simulation was performed using python script vasp_raman.py [8] based on computation the derivative of the polarizability (or macroscopic dielectric tensor) with respect to that normal mode coordinate: dP/dQ (or de/dQ) [9].

4.6 Photocurrent measurement setup

The photoresponse measurements were performed based on a confocal microscopy setup. A ~1 mW 532 nm green laser beam was focused onto a ~450 nm 1/e² radius spot using a 50× microscope objective lens. The sample was mounted on an Autocube scanning stage with a scanning resolution of 100 nm both along x and y directions. The photocurrent at zero source-drain bias was measured using a DC current amplifier and recorded by home-designed Labview software.

Acknowledgements

This work is supported by the United States Department of Energy under Grant DE-SC0014208 and by The National Science Foundation under Grant 1752997. We acknowledge the Coordinated Instrument Facility (CIF) of Tulane University for the support of various instruments. P.B.S. and L.Y.A. (theoretical calculations) were supported by the Russian Science Foundation (Project identifier: 17-72-20223). We are grateful to the supercomputer cluster provided by the Materials Modelling and Development Laboratory at **NUST** (supported via the Grant from the Ministry of Education and Science of the Russian Federation No. 14.Y26.31.0005) and to the Joint Supercomputer Center of the Russian Academy of Sciences.

Electronic Supplementary Material: Supplementary material (further details of solvents selections, X-ray diffraction spectrum, AFM images of thinnest TPdS nanowires, simulated vibrational modes and Raman spectra, and stability analysis) is available in the online version of this article at http://dx.doi.org/10.1007/s12274-***-***-*

References

- K. S. Novoselov, A. K. Geim, S. V. Morozov, D. Jiang, Y. Zhang, S. V. Dubonos, I. V. Grigorieva, A. A. Firsov, Electric field effect in atomically thin carbon films. *Science* 306, 666-669 (2004).
- [2] K. S. Novoselov, Z. Jiang, Y. Zhang, S. V. Morozov, H. L. Stormer, U. Zeitler, J. C. Maan, G. S. Boebinger, P. Kim, A. K. Geim, Room-temperature quantum hall effect in graphene. *Science* 315, 1379-1379 (2007).
- [3] A. K. Geim, K. S. Novoselov, The rise of graphene. *Nat Mater* 6, 183-191 (2007).
- [4] C. R. Dean, A. F. Young, I. Meric, C. Lee, L. Wang, S. Sorgenfrei, K. Watanabe, T. Taniguchi, P. Kim, K. L. Shepard, J. Hone, Boron nitride substrates for high-quality graphene electronics. *Nat Nanotechnol* 5, 722-726 (2010).
- [5] K. S. Novoselov, D. Jiang, F. Schedin, T. J. Booth, V. V. Khotkevich, S. V. Morozov, A. K. Geim, Two-dimensional atomic crystals. *P Natl Acad Sci USA* 102, 10451-10453 (2005).
- [6] B. Radisavljevic, A. Radenovic, J. Brivio, V. Giacometti, A. Kis, Single-layer MoS₂ transistors. *Nat Nanotechnol* 6, 147-150 (2011).
- [7] S. Das, H. Y. Chen, A. V. Penumatcha, J. Appenzeller, High Performance Multilayer MoS₂ Transistors with Scandium Contacts. *Nano Lett* 13, 100-105 (2013).

- [8] D. Ovchinnikov, A. Allain, Y. S. Huang, D. Dumcenco, A. Kis, Electrical Transport Properties of Single-Layer WS₂. Acs Nano 8, 8174-8181 (2014).
- [9] X. Liu, J. Hu, C. L. Yue, N. Della Fera, Y. Ling, Z. Q. Mao, J. Wei, High Performance Field-Effect Transistor Based on Multi layer Tungsten Disulfide. Acs Nano 8, 10396-10402 (2014).
- [10] L. K. Li, Y. J. Yu, G. J. Ye, Q. Q. Ge, X. D. Ou, H. Wu, D. L. Feng, X. H. Chen, Y. B. Zhang, Black phosphorus field-effect transistors. *Nat Nanotechnol* 9, 372-377 (2014).
- [11] X. Liu, J. Y. Liu, L. Y. Antipina, J. Hu, C. L. Yue, A. M. Sanchez, P. B. Sorokin, Z. Q. Mao, J. Wei, Direct Fabrication of Functional Ultrathin Single-Crystal Nanowires from Quasi-One-Dimensional van der Waals Crystals. *Nano Lett* 16, 6188-6195 (2016).
- [12] M. A. Stolyarov, G. X. Liu, M. A. Bloodgood, E. Aytan, C. L. Jiang, R. Samnakay, T. T. Salguero, D. L. Nika, S. L. Rumyantsev, M. S. Shur, K. N. Bozhilov, A. A. Balandin, Breakdown current density in h-BN-capped quasi-1D TaSe₃ metallic nanowires: prospects of interconnect applications. *Nanoscale* 8, 15774-15782 (2016).
- [13] G. X. Liu, S. Rumyantsev, M. A. Bloodgood, T. T. Salguero, M. Shur, A. A. Balandin, Low-Frequency Electronic Noise in Quasi-1D TaSe₃ van der Waals Nanowires. *Nano Lett* 17, 377-383 (2017).
- [14] B. Peng, K. Xu, H. Zhang, Z. Y. Ning, H. Z. Shao, G. Ni, J. Li, Y. Y. Zhu, H. Y. Zhu, C. M. Soukoulis, 1D SbSeI, SbSI, and SbSBr With High Stability and Novel Properties for Microelectronic, Optoelectronic, and Thermoelectric Applications. *Advanced Theory and Simulations* 1, 1700005 (2018).
- [15] A. Geremew, M. A. Bloodgood, E. Aytan, B. W. K. Woo, S. R. Corber, G. Liu, K. N. Bozhilov, T. T. Salguero, S. Rumyantsev, M. P. Rao, A. A. Balandin, Current carrying capacity of quasi-1D ZrTe₃ van der Waals nanoribbons. *IEEE Electron Device Letters* 39, 735-738 (2018).
- [16] M. A. Bloodgood, P. Wei, E. Aytan, K. N. Bozhilov, A. A. Balandin, T. T. Salguero, Monoclinic structures of niobium trisulfide. *APL Materials* 6, 026602 (2018).
- [17] A. Geremew, F. Kargar, E. X. Zhang, S. E. Zhao, E. Aytan, M. A. Bloodgood, T. T. Salguero, S. Rumyantsev, A. Fedoseyev, D. M. Fleetwood, A. A. Balandin, Proton-irradiation-immune electronics implemented with two-dimensional charge-density-wave devices. *Nanoscale* 11, 8380-8386 (2019).
- [18] D. Fox, Y. Zhou, P. Maguire, A. Neill, C. Coileain, R. Gatensby, A. Glushenkov, T. Tao, G. Duesberg, I. V. Shvets, M. Abid, H. Wu, Y. Chen, J. N. Coleman, J. F. Donegan, H. Zhang, Nanopatterning and Electrical Tuning of MoS₂ Layers with a Subnanometer Helium Ion Beam. *Nano Lett* 15, 5307-5313 (2015).
- [19] M. Stanford, P. Pudasaini, N. Cross, K. Mahady, A. Hoffman, D. Mandrus, G. Duscher, M. Chisholm, P. Rack, Tungsten Diselenide Patterning and Nanoribbon Formation by Gas-Assisted Focused Helium Ion Beam Induced Etching. Small Methods, 1600060 (2017).
- [20] C. Nethravathi, A. Jeffery, M. Rajamathi, N. Kawamoto, R. Tenne, D. Golberg, Y. Bando, Chemical Unzipping of WS₂ nanotubes. *Acs Nano* 7, 7311-7317 (2013).

[21] J. Lin, Z. Peng, G. Wang, D. Zakhidov, E. Rodriguez, M. Yacaman, J. Tour, Enhanced Electrocatalysis for Hydrogen Evolution Reactions from WS2 Nanoribbons. Advanced Energy Materials 4, 1301875 (2014).

- [22] Y. Hernandez, V. Nicolosi, M. Lotya, F. M. Blighe, Z. Y. Sun, S. De, I. T. McGovern, B. Holland, M. Byrne, Y. K. Gun'ko, J. J. Boland, P. Niraj, G. Duesberg, S. Krishnamurthy, R. Goodhue, J. Hutchison, V. Scardaci, A. C. Ferrari, J. N. Coleman, High-yield production of graphene by liquid-phase exfoliation of graphite. Nat Nanotechnol 3, 563-568 (2008).
- [23] J. N. Coleman, M. Lotya, A. O'Neill, S. D. Bergin, P. J. King, U. Khan, K. Young, A. Gaucher, S. De, R. J. Smith, I. V. Shvets, S. K. Arora, G. Stanton, H. Y. Kim, K. Lee, G. T. Kim, G. S. Duesberg, T. Hallam, J. J. Boland, J. J. Wang, J. F. Donegan, J. C. Grunlan, G. Moriarty, A. Shmeliov, R. J. Nicholls, J. M. Perkins, E. M. Grieveson, K. Theuwissen, D. W. McComb, P. D. Nellist, V. Nicolosi, Two-Dimensional Nanosheets Produced by Liquid Exfoliation of Layered Materials. Science 331, 568-571 (2011).
- [24] R. J. Smith, P. J. King, M. Lotya, C. Wirtz, U. Khan, S. De, A. O'Neill, G. S. Duesberg, J. C. Grunlan, G. Moriarty, J. Chen, J. Z. Wang, A. I. Minett, V. Nicolosi, J. N. Coleman, Large-Scale Exfoliation of Inorganic Layered Compounds in Aqueous Surfactant Solutions. Adv Mater 23, 3944-3948 (2011).
- [25] J. R. Brent, N. Savjani, E. A. Lewis, S. J. Haigh, D. J. Lewis, P. O'Brien, Production of few-layer phosphorene by liquid exfoliation of black phosphorus. Chem Commun 50, 13338-13341 (2014).
- [26] P. Yasaei, B. Kumar, T. Foroozan, C. H. Wang, M. Asadi, D. Tuschel, J. E. Indacochea, R. F. Klie, A. Salehi-Khojin, High-Quality Black Phosphorus Atomic Layers by Liquid-Phase Exfoliation. Adv Mater 27, 1887-1892 (2015).
- [27] C. Y. Zhi, Y. Bando, C. C. Tang, H. Kuwahara, D. Golberg, Large-Scale Fabrication of Boron Nitride Nanosheets and Their Utilization in Polymeric Composites with Improved Thermal and Mechanical Properties. Adv Mater 21, 2889-2893 (2009).
- [28] J. H. Warner, M. H. Rummeli, A. Bachmatiuk, B. Buchner, Atomic Resolution Imaging and Topography of Boron Nitride Sheets Produced by Chemical Exfoliation. Acs Nano 4, 1299-1304 (2010).
- [29] A. G. Kelly, T. Hallam, C. Backes, A. Harvey, A. S. Esmaeily, I. Godwin, J. Coelho, V. Nicolosi, J. Lauth, A. Kulkarni, S. Kinge, L. D. A. Siebbeles, G. S. Duesberg, J. N. Coleman, All-printed thin-film transistors from networks of liquid-exfoliated nanosheets. Science 356, 69-72 (2017).
- [30] J. Liu, M. J. Casavant, M. Cox, D. A. Walters, P. Boul, W. Lu, A. J. Rimberg, K. A. Smith, D. T. Colbert, R. E. Smalley, Controlled deposition of individual single-walled carbon nanotubes on chemically functionalized templates. Chem Phys Lett 303, 125-129 (1999).
- [31] S. D. Bergin, V. Nicolosi, P. V. Streich, S. Giordani, Z. Y. Sun, A. H. Windle, P. Ryan, N. P. P. Niraj, Z. T. T. Wang, L. Carpenter, W. J. Blau, J. J. Boland, J. P. Hamilton, J. N. Coleman, Towards solutions of single-walled carbon nanotubes in common solvents. Adv Mater 20, 1876-1881 (2008)

- [32] J. N. Coleman, Liquid-Phase Exfoliation of Nanotubes and Graphene. Adv Funct Mater 19, 3680-3695 (2009).
- [33] O. Cao, S. J. Han, G. S. Tulevski, A. D. Franklin, W. Haensch, Evaluation of field-effect mobility and contact resistance of transistors that use solution-processed single-walled carbon nanotubes. Acs Nano 6, 6471-6477 (2012).
- [34] M. S. Fuhrer, B. M. Kim, T. Durkop, T. Brintlinger, High-mobility nanotube transistor memory. Nano Lett 2, 755-759 (2002).
- [35] T. Durkop, S. A. Getty, E. Cobas, M. S. Fuhrer, Extraordinary mobility in semiconducting nanotubes. Nano Lett 4, 35-39 (2004).
- [36] S. J. Kang, C. Kocabas, T. Ozel, M. Shim, N. Pimparkar, M. A. Alam, S. V. Rotkin, J. A. Rogers, High-performance electronics using dense, perfectly aligned arrays of single-walled barbon nanotubes. Nat Nanotechnol 2, 230-236 (2007).
- [37] Q. Cao, H. Kim, N. Pimparkar, J. P. Kulkarni, C. J. Wang, M. Shim, K. Roy, M. A. Alam, J. A. Rogers, Medium-scale carbon nanotube thin-film integrated circuits on flexible plastic substrates. Nature 454, 495-500 (2008).
- [38] Y. Cui, Z. Zhang, D. Wang, W. U. Wang, C. M. Lieber, High performance silicon nanowire field effect transistors. Nano Lett 3, 149-152 (2003).
- [39] X. Duan, C. Niu, V. Sahi, J. Chen, J. W. Parce, S. Empedocles, J. L. Goldman, High-performance thin-film transistors using semiconductor nanowires and nanoribbons. Nature 425, 274-278 (2003).
- [40] M. S. Tang, E. P. Ng, J. C. Juan, C. W. Ooi, T. C. Ling, K. L. Woon, P. L. Show, Metallic and semiconducting carbon nanotubes separation using an aqueous two-phase separation technique: a review. Nanotechnology 27, 332002 (2016).
- [41] J. F. Shen, Y. M. He, J. J. Wu, C. T. Gao, K. Keyshar, X. Zhang, Y. C. Yang, M. X. Ye, R. Vajtai, J. Lou, P. M. Ajayan, Liquid Phase Exfoliation of Two-Dimensional Materials by Directly Probing and Matching Surface Tension Components. *Nano Lett* **15**, 5449-5454 (2015).
- [42] Y. Zhao, X. Luo, H. Li, J. Zhang, P. T. Araujo, C. K. Gan, J. Wu, H. Zhang, S. Y. Quek, M. S. Dresselhaus, Q. H. Xiong, Interlayer breathing and shear modes in few-trilayer MoS2 and WSe2. Nano Lett 13, 1007-1015 (2013).
- [43] R. Claus, H. H. Hacker, H. W. Schrotter, J. Brandmuller, S. Haussuhl, Low-Frequency Optical-Phonon Spectrum Of Benzil. Phys Rev 187, 1128 (1969).
- [44] Z. Q. Ren, L. E. McNeil, S. B. Liu, C. Kloc, Molecular motion and mobility in an organic single crystal: Raman study and model. Phys Rev B 80, 245211 (2009).
- [45] H. Q. Ye, G. F. Liu, S. Liu, D. Casanova, X. Ye, X. T. Tao, Q. C. Zhang, Q. H. Xiong, Molecular-Barrier-Enhanced Aromatic Fluorophores in Cocrystals with Unity Quantum Efficiency. Angew Chem Int Edit 57, 1928-1932 (2018).
- [46] J. Kim, J. U. Lee, J. Lee, H. J. Park, Z. Lee, C. Lee, H. Cheong, Anomalous polarization dependence of Raman scattering and crystallographic orientation of black phosphorus. Nanoscale 7, 18708-18715 (2015).
- [47] D. Braga, I. G. Lezama, H. Berger, A. F. Morpurgo, Quantitative Determination of the Band Gap of WS2 with

- Ambipolar Ionic Liquid-Gated Transistors. *Nano Lett* 12, 5218-5223 (2012).
- [48] K. Lee, H. Y. Kim, M. Lotya, J. N. Coleman, G. T. Kim, G. S. Duesberg, Electrical Characteristics of Molybdenum Disulfide Flakes Produced by Liquid Exfoliation. Adv. Mater 23, 4178-4182 (2011).
- [49] J. K. Kang, J. D. Wood, S. A. Wells, J. H. Lee, X. L. Liu, K. S. Chen, M. C. Hersam, Solvent Exfoliation of Electronic-Grade, Two-Dimensional Black Phosphorus. Acs Nano 9, 3596-3604 (2015).
- [50] W. J. Kim, C. Y. Lee, K. P. O'Brien, J. J. Plombon, J. M. Blackwell, M. S. Strano, Connecting single molecule electrical measurements to ensemble spectroscopic properties for quantification of single-walled carbon nanotube separation. J. Am. Chem. Soc. 131, 3128-3129 (2009).
- [51] W. M. Wang, C. LeMieux, S. Selvarasah, M. R. Dokmeci, Z. N. Bao, Dip-Pen Nanolithography of Electrical Contacts to Single-Walled Carbon Nanotubes. *Acs Nano* 3, 3543-3551 (2009).
- [52] Y. Ahn, J. Dunning, J. Park, Scanning photocurrent imaging and electronic band studies in silicon nanowire field effect transistors. *Nano Lett* 5, 1367-1370 (2005).
- [53] M. Freitag, J. C. Tsang, A. Bol, P. Avouris, D. N. Yuan, J. Liu, Scanning photovoltage microscopy of potential modulations in carbon nanotubes. *Appl Phys Lett* 91, 031101 (2007).
- [54] P. Avouris, M. Freitag, V. Perebeinos, Carbon-nanotube photonics and optoelectronics. *Nat Photonics* 2, 341-350 (2008).
- [55] H. Kind, H. Q. Yan, B. Messer, M. Law, P. D. Yang, Nanowire ultraviolet photodetectors and optical switches. *Adv Mater* 14, 158-160 (2002).
- [56] Z. J. Li, Z. P. Hu, J. Peng, C. Z. Wu, Y. C. Yang, F. Feng, P. Gao, J. L. Yang, Y. Xie, Ultrahigh Infrared Photoresponse from Core-Shell Single-Domain-VO₂/V₂O₅ Heterostructure in Nanobeam. *Adv Funct Mater* 24, 1821-1830 (2014).
- [57] J. M. Wu, W. E. Chang, Ultrahigh Responsivity and External Quantum Efficiency of an Ultraviolet-Light Photodetector Based on a Single VO₂ Microwire. Acs Appl Mater Inter 6, 14286-14292 (2014).
- [58] D. Sun, G. Aivazian, A. M. Jones, J. S. Ross, W. Yao, D. Cobden, X. D. Xu, Ultrafast hot-carrier-dominated photocurrent in graphene. *Nat Nanotechnol* 7, 114-118 (2012)
- [59] M. Buscema, D. J. Groenendijk, S. I. Blanter, G. A. Steele, H. S. J. van der Zant, A. Castellanos-Gomez, Fast and Broadband Photoresponse of Few-Layer Black Phosphorus Field-Effect Transistors. *Nano Lett* 6, 3347-3352 (2014).
- [60] Z. Y. Yin, H. Li, H. Li, L. Jiang, Y. M. Shi, Y. H. Sun, G. Lu, Q. Zhang, X. D. Chen, H. Zhang, Single-Layer MoS₂ Phototransistors. Acs Nano 6, 74-80 (2012).
- [61] W. Choi, M. Y. Cho, A. Konar, J. H. Lee, G. B. Cha, S. C. Hong, S. Kim, J. Kim, D. Jena, J. Joo, S. Kim, High-detectivity multilayer MoS₂ phototransistors with spectral response from ultraviolet to infrared. *Adv Mater* 24, 5832-5836 (2012).
- [62] N. Perea-Lopez, A. L. Elias, A. Berkdemir, A. Castro-Beltran, H. R. Gutierrez, S. Feng, R. Lv, T. Hayashi,

- F. Lopez-Urias, S. Ghosh, B. Muchharla, S. Talapatra, H. Terrones, M. Terrones, Photosensor Device Based on Few-Layered WS₂ films. *Adv Funct Mater* **23**, 5511-5517 (2013).
- [63] O. Lopez-Sanchez, D. Lembke, M. Kayci, A. Radenovic, A. Kis, Ultrasensitive photodetectors based on monolayer MoS₂. Nat Nanotechnol 8, 497-501 (2013).
- [64] D. J. Groenendijk, M. Buscema, G. A. Steele, S. M. Vasconcellos, R. Bratschitsch, H. S. J. van der Zant, A. Castellanos-Gomez, Photovoltaic and Photothermoelectric Effect in a Double-Gated WSe₂ Device. *Nano Lett* 14, 5846-5852 (2014).
- [65] T. Y. Zhai, X. S. Fang, M. Y. Liao, X. J. Xu, H. B. Zeng, B. Yoshio, D. Golberg, A Comprehensive Review of One-Dimensional Metal-Oxide Nanostructure Photodetectors. Sensors 9, 6504-6529 (2009).
- [66] R. Tamang, B. Varghese, S. G. Mhaisalkar, E. S. Tok, C. H. Sow, Probing the photoresponse of individual Nb₂O₅ nanowires with global and localized laser beam irradiation. *Nanotechnology* 22, 115202 (2011).
- [67] M. M. Furchi, A. Pospischil, F. Libisch, J. Burgdorfer, T. Mueller, Photovoltaic Effect in an Electrically Tunable van der Waals Heterojunction. *Nano Lett* 14, 4785-4791 (2014).
- [68] C. H. Lee, G. H. Lee, A. M. van der Zande, W. C. Chen, Y. L. Li, M. Y. Han, X. Cui, G. Arefe, C. Nuckolls, T. F. Heinz, J. Guo, J. Hone, P. Kim, Atomically thin p-n junctions with van der Waals heterointerfaces. *Nat Nanotechnol* 9, 676-681 (2014).
- [69] M. Buscema, M. Barkelid, V. Zwiller, H. S. J. van der Zant, G. A. Steele, A. Castellanos-Gomez, Large and Tunable Photothermoelectric Effect in Single-Layer MoS₂. *Nano Lett* 13, 358-363 (2013).
- [70] K. Balasubramanian, Y. W. Fan, M. Burghard, K. Kern, M. Friedrich, U. Wannek, A. Mews, Photoelectronic transport imaging of individual semiconducting carbon nanotubes. *Appl Phys Lett* 84, 2400-2402 (2004).
- [71] A. W. Tsen, L. A. K. Donev, H. Kurt, L. H. Herman, J. Park, Imaging the electrical conductance of individual carbon nanotubes with photothermal current microscopy. *Nat Nanotechnol* 4, 108-113 (2009).
- [72] G. Buchs, S. Bagiante, G. A. Steele, Identifying signatures of photothermal current in a double-gated semiconducting nanotube (vol 5, 4987, 2014). *Nat Commun* 6, (2015).
- [73] Y. H. Ahn, A. W. Tsen, B. Kim, Y. W. Park, J. Park, Photocurrent imaging of p-n junctions in ambipolar carbon nanotube transistors. *Nano Lett* 7, 3320-3323 (2007).

Methods Reference

- [1] Hohenberg, P. & Kohn, W. Inhomogeneous electron gas. *Phys. Rev.* 136, 864-871 (1964).
- [2] Kohn, W. & Sham, L. J. Self-consistent equations including exchange and correlation effects. *Phys. Rev.* 140, 1133-1138 (1965).
- [3] Perdew, J. P., Burke, K. & Ernzerhof, M. Generalized Gradient Approximation Made Simple. *Phys. Rev. Lett.* 77, 3865-3868 (1996).
- [4] Kresse, G. & Hafner, J. Ab initio molecular dynamics for liquid metals. *Phys. Rev. B* 47, 558–561 (1993).

[5] Kresse, G. & Hafner, J. Ab initio molecular-dynamics simulation of the liquid-metal-amorphous-semiconductor transition in germanium. Phys. Rev. B 49, 14251-14269 (1994).

- Kresse, G. & Furthmüller, J. Efficient iterative schemes for ab initio total-energy calculations using a plane-wave basis set. Phys. Rev. B 54, 11169-11186 (1996).
- [7] Monkhorst, H. J. & Pack, J. D. Special points for Brillouin-zone integrations. Phys. Rev. B 13, 5188-5192
- (1976).
- [8] Fonari, A. & Stauffer, S. vasp_raman.py. (https://github.com/raman-sc/VASP/, 2013).
- Porezag, D. & Pederson, M. R. Infrared intensities and Raman-scattering activities within density-functional theory. Phys. Rev. B 54, 7830-7836 (1996).

Electronic Supplementary Material

High yield production of ultrathin fibroid semiconducting nanowire of Ta₂Pd₃Se₈

Xue Liu,^{1, 2} Sheng Liu,² Liubov Yu. Antipina,^{3, 5, 6} Yibo Zhu,⁷ Jinliang Ning,¹ Jinyu Liu,¹ Chunlei Yue,¹ Abin Joshy,¹ Yu Zhu,⁴ Jianwei Sun,¹ Ana M Sanchez,⁸ Pavel B. Sorokin,^{3, 5} Zhiqiang Mao,¹ Qihua Xiong,² and Jiang Wei¹ (🖂)

Supporting information to DOI 10.1007/s12274-****-* (automatically inserted by the publisher)

Supplementary Note 1. Solvents selections for the Ta₂Pd₃Se₈ (TPdS) liquid phase exfoliations.

Basically, the well accepted theory or strategy to find a proper solvent for liquid phase exfoliation is the surface tension matching between solute and solvent, i.e. a lower difference of surface tension between solvents and low dimensional materials will result in a better liquid phase exfoliation process. However, it was found by Coleman and coworkers that the surface tension can only be used for initial screening of proper solvents [1, 2]. Although with a matched surface tension, more complicated parameters are needed to further evaluate the process more precisely. For example, as proposed by Jianfeng et al., different surface tension components including dispersive component and polar component can be used to further select the solvents [3]. Thus, a proper liquid exfoliation process not only requires a matching of the total surface tension, but also relies on the matching of each component, i.e. the matching of polar component may correlate to the ability to separate nanostructures from the bulk counterparts through dipole interactions, while the matching of dispersive component gives rise to a stable dispersion after succeed exfoliation [3, 4].

In our experiments, the NMP solvent provides better liquid phase exfoliation results, referring to as well dispersed TPdS-NMP mixtures without clear aggregation over a certain period of time. The other solvents as used in our experiments are not appropriate: they are either inefficient to separate TPdS nanowires (Chloroform and Hexane) or easy to form aggregation (Acetone and IPA). We propose our understanding as the following. Firstly, the polar component of surface tension is related to the polar interactions which comprise Coulomb interactions between permanent dipoles and/or induced dipoles (e.g. hydrogen bonds), while the dispersive component reflects the interactions caused by temporary fluctuations of the charge distribution in atoms/molecules (e.g. van der Waals interactions). Since our TPdS nanowires are randomly separated from

¹ Department of Physics and Engineering Physics, Tulane University, New Orleans, Louisiana 70118, United States

² Division of Physics and Applied Physics, Nanyang Technological University, 637371, Singapore

³ National University of Science and Technology "MISiS," Moscow 119049, Russian Federation

⁴ Department of Polymer Science, The University of Akron, Akron, Ohio 44325, United States

⁵ Technological Institute for Superhard and Novel Carbon Materials, Moscow 108840, Russian Federation

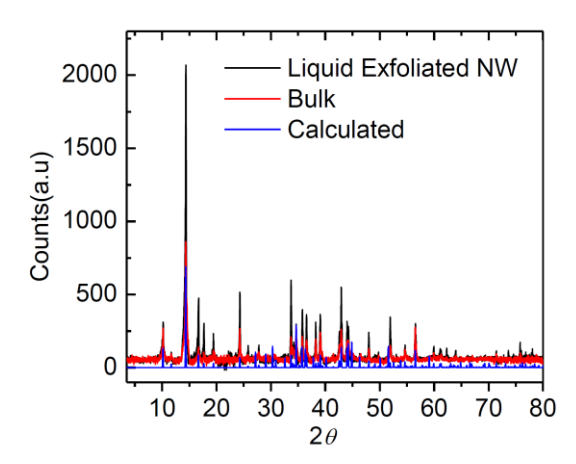
⁶ Moscow Institute of Physics and Technology, Dolgoprudny 141700, Russian Federation

⁷ Department of Mechanical Engineering, Columbia University, New York, New York 10027, United States

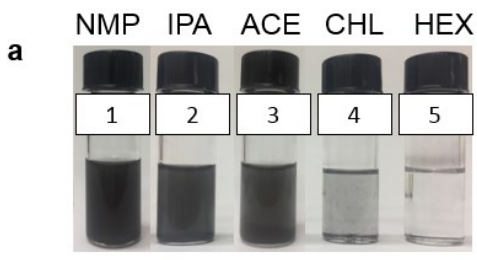
⁸ Department of Physics, University of Warwick, Coventry, CV4 7AL, United Kingdom

their bulk counterparts, a certain level of polar component is expected (i.e. polar interactions caused by the structure asymmetry). Thus, solvents with relatively smaller polar component (< 0.1 polar/dispersive ratio for Chloroform and Hexane) may induce large mismatching with the TPdS nanowires. Then, regarding the stability of the exfoliated mixtures, the dispersive component may play a more important rule. According to our results, IPA and acetone exfoliated mixtures are less stable than NMP, i.e. clear aggregations have formed after a few hours (IPA is slightly better than acetone). This may due to a mismatched dispersive component of the surface tension as compared with the TPdS nanowires (IPA with 19.50 mJ·m⁻² is more close to NMP of 29.21 mJ·m⁻² than Acetone of 16.50 mJ·m⁻²). As we know, the dispersive component is closely related to the interactions caused by temporary fluctuations of the charge distribution in atoms/molecules (e.g. van der Waals interactions) [4]. When the TPdS nanowires are dispersed in a certain solvent, stable van der Waals interactions between solute and solvent molecules are expected. So, a well matched dispersive component may give rise to a thermodynamically stabilized mixture.

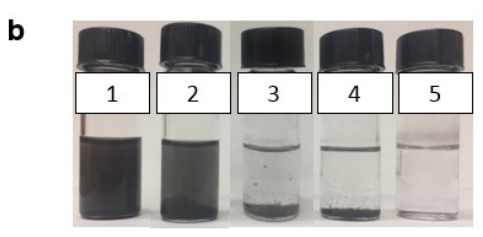
Overall, the NMP solvent is supposed to better fit with our TPdS nanowires due to matched surface tension and different components, however, the accurate values for TPdS nanowires are still unknown. Indeed, the real condition may be more complicated, since the surface tension and corresponded components can also depend on their dimension and size distributions. Thus, it requires more comprehensive thermodynamic analysis to study the best soluble condition for our TPdS nanowires when the TPdS nanowires are dispersed in a certain solvents, the matched dispersive component may give rise to thermodynamically stabilized van der Waals interactions between solute and solvent.



Supplementary Figure 1 X-ray diffraction patterns for Ta₂Pd₃Se₈ materials. Black, red, blue lines correspond to powder XRD spectra obtained from bulk crystal, liquid exfoliated nanowires, and simulated results. They all show great consistency.



Right after exfoliation

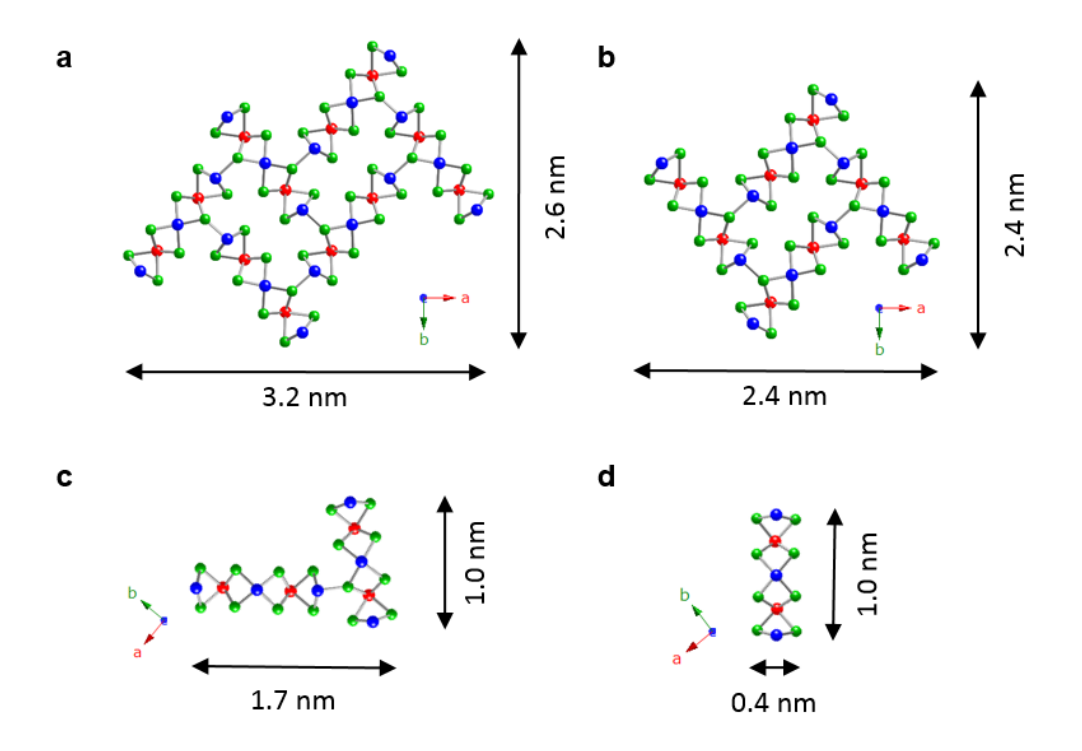


4 hours after exfoliation

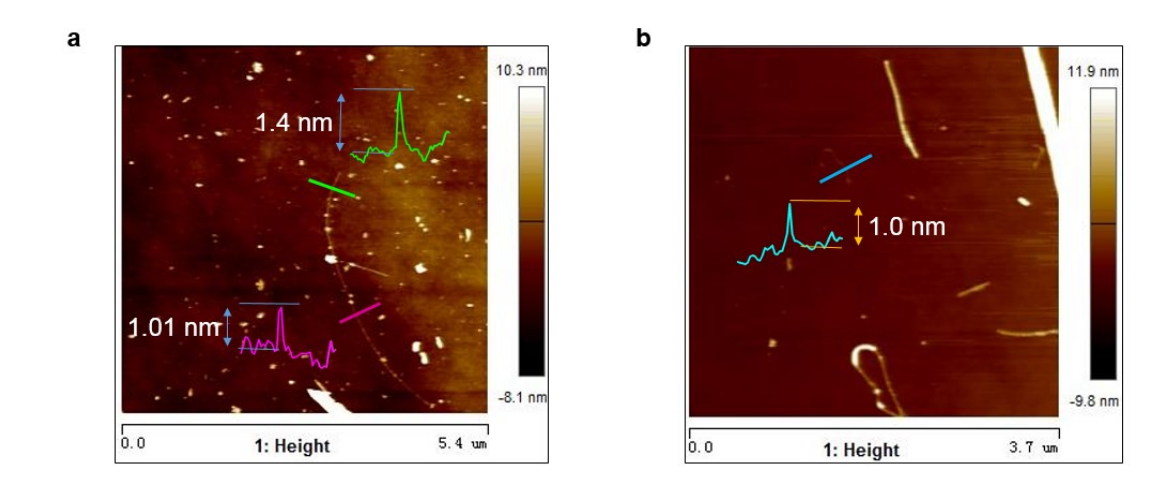
Supplementary Figure 2 Liquid phase exfoliation results of Ta₂Pd₃Se₈ nanowires with different solvents. Images of resultant Ta₂Pd₃Se₈ nanowire dispersions for (a) right after exfoliation and (b) four hours after exfoliation. From 1 to 5 as labeled represent N-methyl-2-pyrrolidone (NMP), Isopropyl alcohol (IPA), Acetone (ACE), Chloroform (CHL), and Hexane (HEX), respectively.

Solvents	Surface tension/	Dispersive component/	Polar component/	Polar component/ Dispersive
	mJ·m⁻²	mJ·m⁻²		component
N-methyl-2-p yrrolidone	40.79	29.21	11.58	0.396
Isopropanol	23.00	19.50	3.50	0.179
Acetone	23.30	16.50	6.80	0.412
Chloroform	27.50	25.90	1.60	0.062
Hexane	18.43	18.43	0.00	0.000

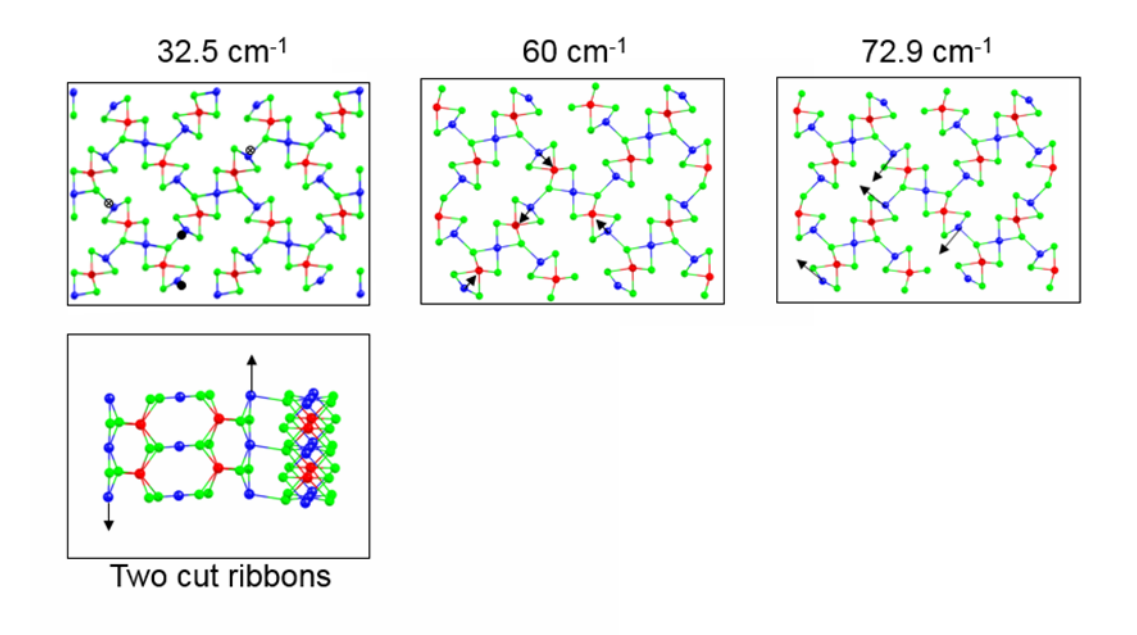
Supplementary Table 1 Parameters of different solvents used in our liquid exfoliations. Note: from our exfoliation results, chloroform and hexane are not able to effectively separate the TPdS nanowires. N-methyl-2-pyrrolidone gives the best exfoliation results with well-dispersed and stable NMP-TPdS mixtures.



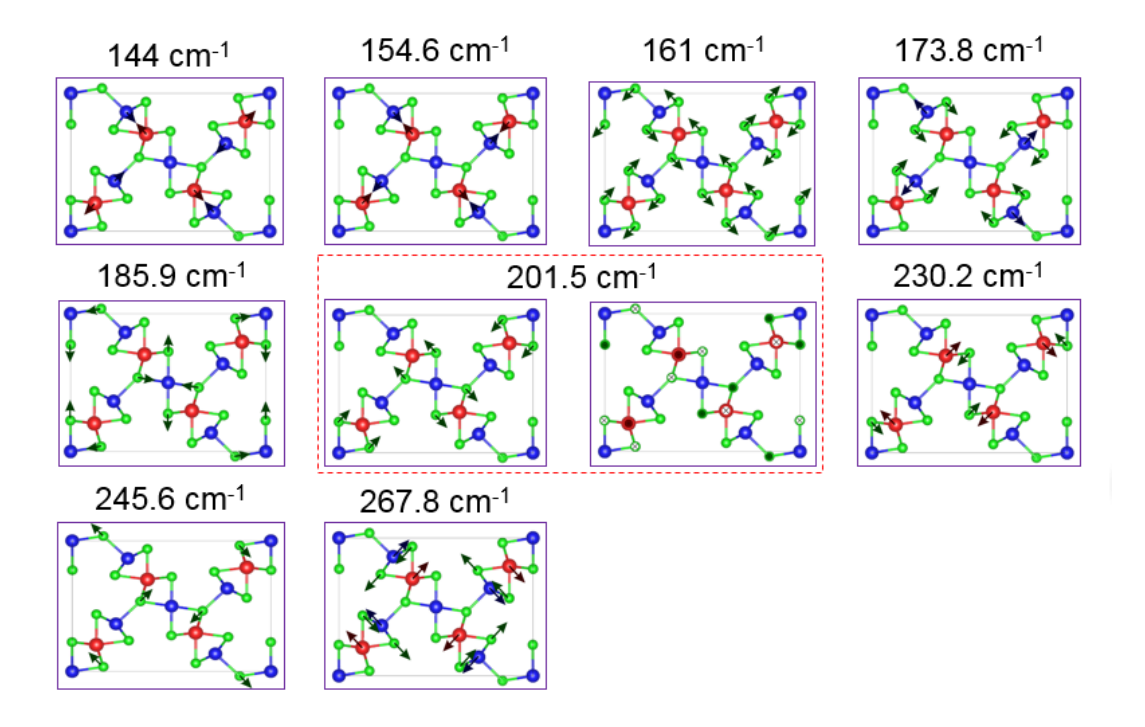
Supplementary Figure 3 Simulated lateral dimensions of Ta₂Pd₃Se₈ nanostructures consisting of a) six, b) four, c) two, and d) single chain, respectively. Note, the simulated cross-sectional dimensions do not reflect the real measured nanowire thickness on silicon wafer, since we have not considered the preferred faces of the TPS nanostructures when deposited onto substrate.



Supplementary Figure 4 Atomic Force Microscopy images of ultra-thin (\sim 1 nm) Ta₂Pd₃Se₈ nanowires produced by NMP liquid exfoliation.



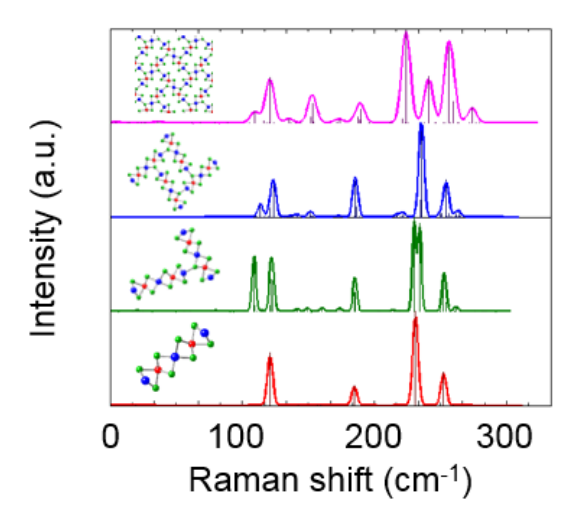
Supplementary Figure 5 Simulated inter-ribbon vibrational modes corresponding to as measured low wavenumber Raman peaks at 32.5 cm⁻¹, 60 cm⁻¹, and 72.9 cm⁻¹.



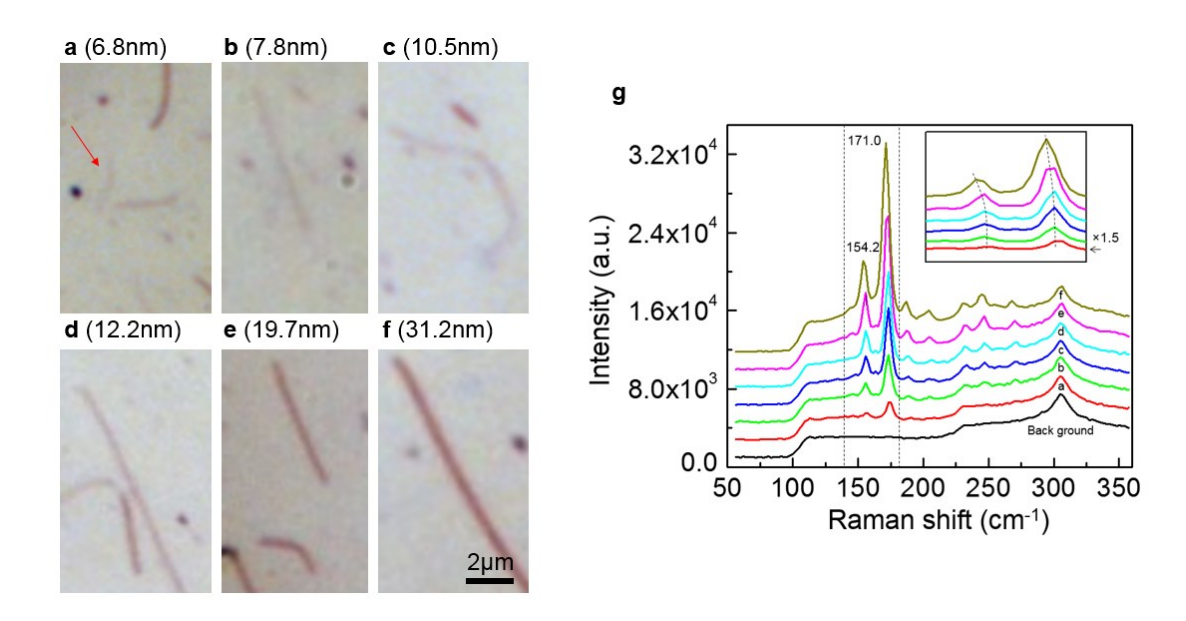
Supplementary Figure 6 Simulated intra-chain vibrational modes corresponding to as measured high wavenumber Raman peaks.

Measured Raman Peaks (cm ⁻¹)	Intensity at $\bar{z}(xx)z I_a$ (a.u.)	Intensity at $\bar{z}(yx)z I_b$ (a.u.)	$I_{ m b}/I_{ m a}$	Correlated simulation peak (cm ⁻¹)
18.3	N/A	76.8	N/A	N/A
26.6	N/A	47.4	N/A	25.73
32.6	174	28.2	0.162	26.47
60.0	269.8	32.6	0.121	53.33
73.2	24	46.8	1.95	53.53
144	14	70.3	5.02	142
154.6	725.6	32	0.04	150
161	226.5	0	0	161
173.8	1876.9	145.5	0.08	174
185.9	165	30.3	0.184	190
201.5	58.1	66.6	1.15	200 or 202
230.2	127.4	0	0	230
245.6	130.3	67.2	0.516	242
267.8	136.8	0	0	265

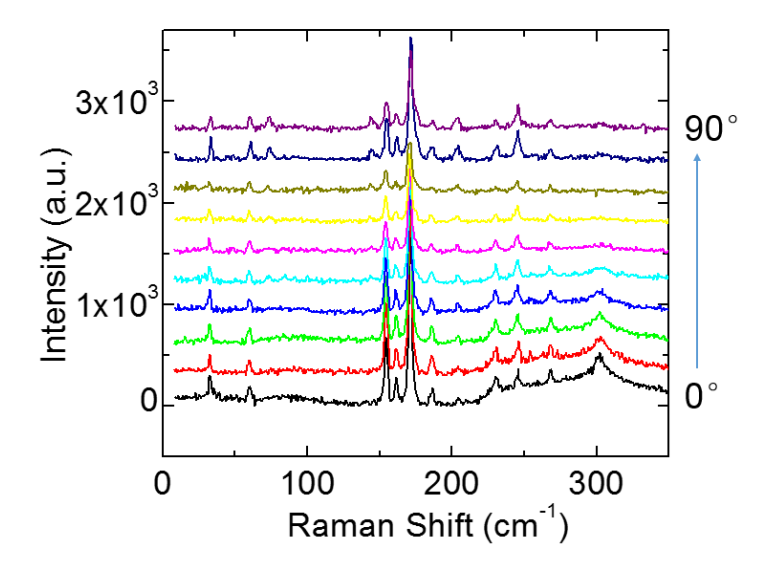
Supplementary Table 2 Table of as measured Raman peak positions, intensity at parallel configuration (I_a), intensity at perpendicular configuration (I_b), I_b/I_a ratio, and possible correlated peaks from simulation. Note, as can be seen from the ratio between I_b and I_a , most of the measured peaks shows a value less than 1, except 73.2 cm⁻¹, 144 cm⁻¹, and 201.5 cm⁻¹.



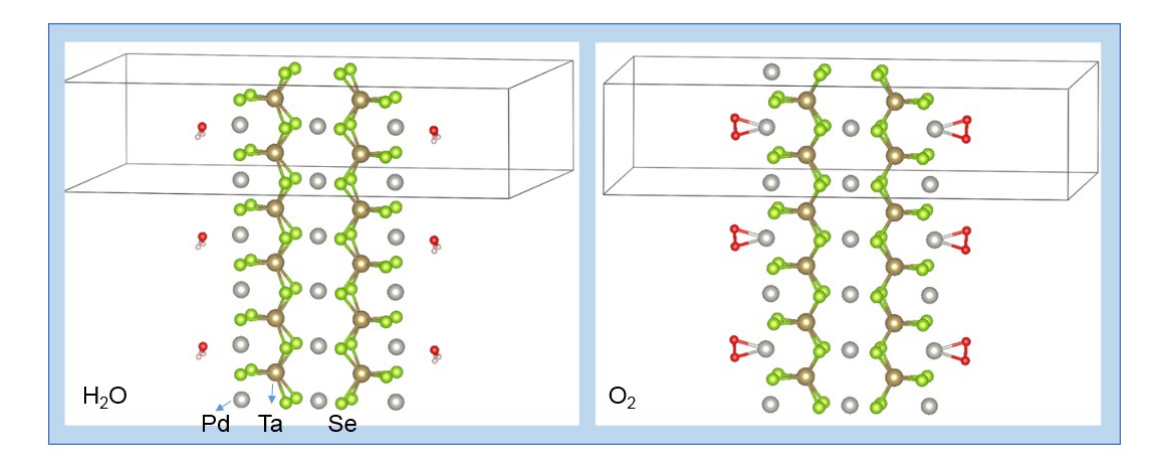
Supplementary Figure 7 Raman spectra evolution with different thicknesses, bulk (pink), four- (blue), two-(green), and single-ribbon (red). Inset: simulated crystal structures corresponding to the spectrum. Note: the four-ribbon nanostructure shows similar Raman spectrum with the bulk, while two- and single-ribbon exhibit unique Raman spectra.



Supplementary Figure 8 Thickness dependent Raman spectra of exfoliated Ta₂Pd₃Se₈ nanowires. a) - f) Optical images of six individual Ta₂Pd₃Se₈ nanowires with different thicknesses, 6.8 nm, 7.8 nm, 10.5 nm, 12.2 nm, 19.7 nm, and 31.2 nm, respectively. g) Raman spectra of Ta₂Pd₃Se₈ nanowires from (a) to (f). Inset, zoom-in view of Raman peaks in the selected range, between dashed lines in (g). Note, the Raman peaks exhibit red shift with reducing thickness, as indicated by 154.2 cm⁻¹ and 171.0 cm⁻¹ peaks in the inset, the dashed curves indicate the evolution.



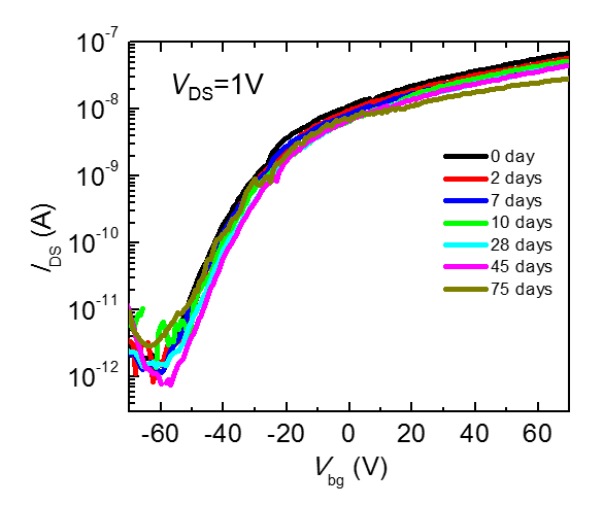
Supplementary Figure 9 Polarization dependent low frequency Raman spectra of a 105 nm Ta₂Pd₃Se₈ nanowire. Note, the polarization dependence of the peak intensities is significant in thin nanowire, which is consistent with the thick Ta₂Pd₃Se₈ sample as shown by Figure 2e in the maintext.



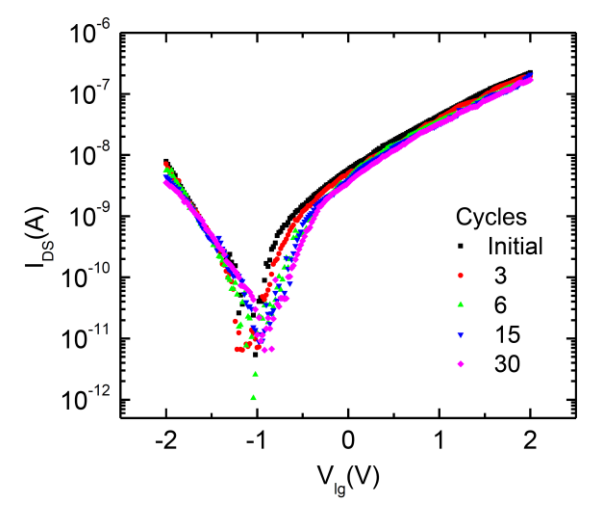
Supplementary Figure 10 H_2O and O_2 molecules adsorptions on $Ta_2Pd_3Se_8$ crystal. Note: the simulated adsorption energies for H_2O and O_2 molecules are -0.33 eV/molecule and 1.12 eV/molecule respectively, and the TPS structural geometry is stable upon such adsorptions.

	MoS_2	Black Phosphrous	Semiconducting	$Ta_2Pd_3Se_8$
			Carbon nanotubes	nanowires
On/off ratio	3-4 [5]	~1.0×10 ³ [6, 7]	$\sim 10^3 [8-10]$	5×10 ² [this work]
Field effect	0.117	0.58~26 [6, 7]	20~200 [8-10]	32.5 [this work]
Mobility	200 (Schottky			
$(cm^2V^{-1}s^{-1})$	barrier			
	removed) [5]			

Supplementary Table 3 Performance comparisons between field-effect transistors based on different channel materials achieved by solution processed liquid phase exfoliation.



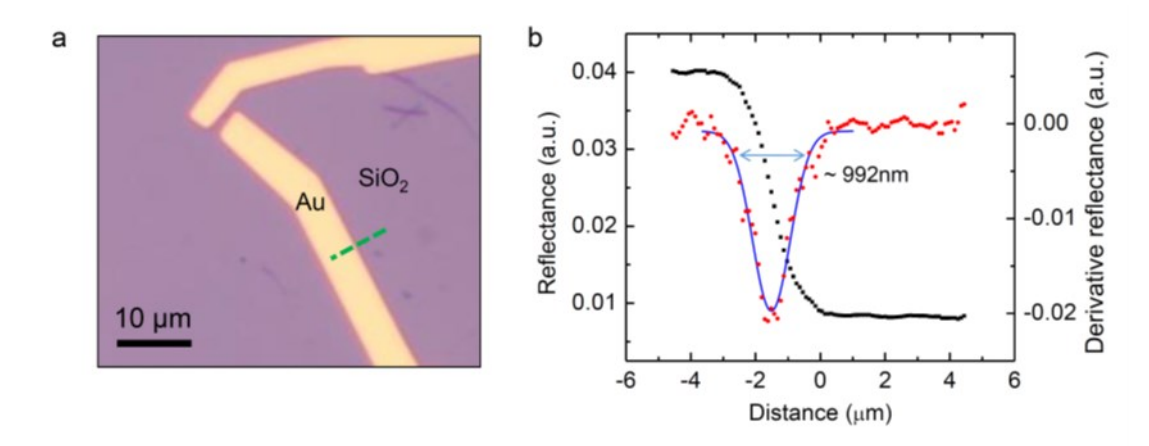
Supplementary Figure 11 Stability analysis of the fabricated Ta₂Pd₃Se₈ 1D transistor via transport measurements. Note, the device was stored in ambient environment for two and a half months without any protection layer on top.



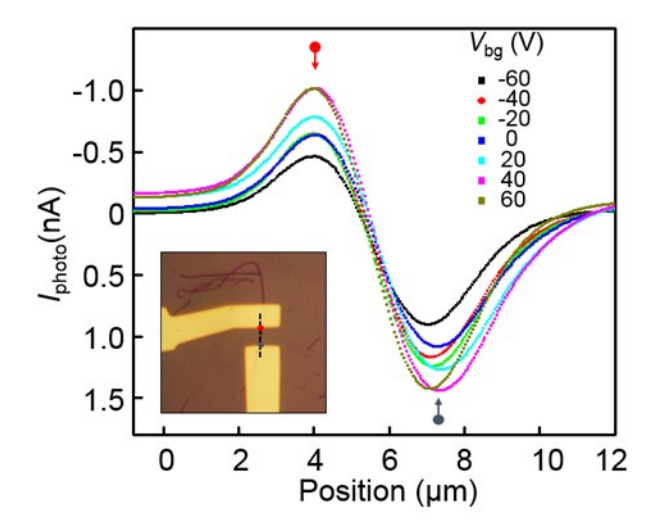
Supplementary Figure 12 Cyclic data for the device performance with a liquid gate.

Supplementary Note 2 Laser spot size determinations.

To estimate the laser spot size, we use the reflectance signal when the laser is scanning over the sharp edge of the Au electrode, as shown by the linecut in Supplementary Figure 13a. The reflected light intensity signal can be viewed as a convolution of the laser intensity profile and the step edge due to different reflectance between metal and SiO₂ surface [11]. By take the derivative of the line profile (Supplementary Figure 13b), we can extract the laser intensity profile. From a Gaussian peak fitting (blue solid line) to the derivative reflectance data (red dots), we obtain a full width at half maximum (FWHM) of ~ 583.7 nm, corresponding to a laser spot $1/e^2$ radius of ~ 496 nm ($2\omega = 1.699 \times FWHM$, where ω is the $1/e^2$ radius).



Supplementary Figure 13 Estimation of laser spot size. a). Optical image of a typical TPdS nanowire photodetector device. b). Laser reflectance profile and its derivative when scanning across gold electrode edge. Blue solid line represents a Gaussian peak fitting to the derivative reflectance signal.



Supplementary Figure 14 Gate dependence of photocurrent profiles along the line cut in the device optical image. Note, when the laser spot is located at the red and blue dots, the photocurrent reaches positive and negative maximum respectively.

Reference

- [1] Hernandez, Y., et. al., Nat. Nanotechnol. 2008, 3, 563-568
- [2] Bergin, S. D., et. al., Advanced Materials, 2008, 20, 1876-1881
- [3] Shen, J. F., et. al., Nano Lett. 2015, 15, 5449-5454
- [4] Owen, D. K. J. Appl. Polym. Sci. 1970, 14, 1725-1730
- [5] Lee, K., et. al., Adv. Mater. 2011, 23, 4178-4182
- [6] Yasaei, P., et. al., Adv. Mater. 2015, 27, 1887
- [7] Kang, J. K., et. al., Acs Nano 2015, 9, 3596
- [8] Cao, Q., et. al., Acs Nano 2012, 6, 6471
- [9] Kim, W. J., et. al., J. Am. Chem. Soc. 2009, 131, 3128
- [10] Wang, W. M., et. al., Acs Nano 2009, 3, 3543
- [11] Buscema, M., et. al., Nano Lett. 2013, 13, 358